AN ANALYTICAL DESIGN OF EXPERIMENTS METHOD FOR FATIGUE CONSTRAINED DESIGN OPTIMIZATION OF A 3D PRINTED STRUCTURE

by

ASHISH POKHAREL

Presented to the Faculty of the Graduate School of

The University of Texas at Arlington in Partial Fulfillment

of the Requirements

for the Degree of

MASTER OF SCIENCE IN MECHANICAL ENGINEERING

THE UNIVERSITY OF TEXAS AT ARLINGTON

December 2018

Copyright © by Ashish Pokharel 2018

All Rights Reserved

Acknowledgements

First, I would like to express my special gratitude to my research supervisor Dr. Robert M. Taylor for providing me with the opportunity to work under his guidance for the completion of my Master of Science degree at University of Texas at Arlington. Without his continuous support, motivation and directions, this research work would not have been possible. I sincerely appreciate him for his valuable time and effort that he has put in to ensure the success of this research. I am also greatly thankful to him for believing in my abilities.

I am very grateful to Dr. Leila Ladani and Dr. Narges Shayesteh Moghaddam for their willingness to provide me valuable suggestions and comments by being a part of my committee. I would also like to acknowledge help provided by Vedant Chahal and I appreciate him for his time and effort. Additionally, I would also like to express my thanks to ANSYS for providing the limited term license for Workbench Additive Suite.

I would like to express my deepest gratitude to my parents for their unconditional love and support and for always believing in me. I am always in debt to my friends who have made United States feel like home away from home.

November 21, 2018

Abstract

AN ANALYTICAL DESIGN OF EXPERIMENTS METHOD FOR FATIGUE CONSTRAINED DESIGN OPTIMIZATION OF 3D PRINTED STRUCTURE

Ashish Pokharel, MS

The University of Texas at Arlington, 2018

Supervising Professor: Robert M. Taylor

A design of experiments approach has been used to analytically determine a low cycle fatigue (LCF) constraint for use in design optimization of 3D printed structures. In context of metal additive manufacturing, the process of melting, solidification and consolidation of metal powder introduces very high temperature gradient field within the build which in turn results in high compressive stresses at the core and tensile stresses at the outer surface of the part after it has cooled down to room temperature post build. An approach of finite element modeling in ANSYS Additive has been used to develop a residual stress profile throughout the build in bridge shaped specimens, keeping the build boundary temperature considerably less than melting temperature of the metal. The effect of these stresses on the fatigue life is predicted using Coffin Manson's model based on plastic strain state produced by high residual stresses superimposed with external loading. Furthermore, equations were developed using linear regression to generate a response surface as a function of span and thickness of the models which could be used for any range of values of these dimensions to represent the fatigue life as well as distortions. With consideration of structural response shown by the specimens, the current work

demonstrates a method in using the developed equations for shape optimization of the printed parts.

Table of Contents

List of Illustrations

List of Tables

Chapter 1

Introduction

Additive manufacturing (AM) is one of the revolutionary cutting-edge technology which enables freeform fabrication of functional 3D components achieving surpass of design restrictions economically, in contrast to the subtractive process (Brackett, et al., 2011) (Vayre, et al., 2012). Additive manufacturing in its early phases of development was primarily used for fabrication of the prototypes of designs and thus, the process was termed as “Rapid Prototyping” or “3D printing”. However, it was not until the capability of this technology was realized that it could produce end use functional parts after which the term “Additive Manufacturing” gained its popularity. With additive, parts featuring any geometric complexity could be produced with considerably less lead time as the steps of tooling and post-processing is either reduced to a minimal extent or eliminated (Gu et al., 2012). Furthermore, the range of materials AM encompasses is from plastics, composites to metals and many more. Due to ability to work with wide range of materials and inherent design flexibility its scope and capability have been realized from part repairs to direct part manufacturing in applications of automotive industry, aerospace industry, medical devices, dental implants, furnitures, fabrics, etc.

In context of metal additive manufacturing especially selective laser melting (SLM), parts with almost 99% density can be achieved with very fine features (Wang, 2012). Despite of this, many challenges have been identified with previous researches which address sensitivity of process parameters to the quality of build that directly impacts parts’ microstructures, anomalies, etc. which may be detrimental to the integrity of structural components (Gorelik, 2017). Additionally, repetitive melting and re-solidification process involved within millions of powder particles impose very high temperature gradient field resulting in residual stresses that have been proven to have deleterious effect in terms of

structural strength of the printed parts (Protasov et al., 2016) (Roberts, 2002). One of the major effects of these stresses is part distortion post-removal off the base plate and supports, thus, compensating geometric accuracy of the part that might be critical in case of load bearing structures and assemblies. On the other hand, these stresses are also detrimental to fatigue life of the structural components due to the superposition effect with externally applied loads.

Realizing the potential of additive manufacturing to surpass design complexity, the conventional designs are being modified in order to leverage lightweight structures using topology optimization in combination with shape and size optimization enabling reduction of mass of the component maintaining its structural integrity. This report is primarily focused on using an approach of design of experiments to establish a low cycle fatigue and distortion constraint which can be used in design optimization of 3D printed structures. An approach of finite element modeling in ANSYS Additive has been used to develop residual stress profile throughout the build in bridge shaped specimens to predict the distortions. The effect of these stresses on the low cycle fatigue regime is predicted using Coffin Manson's model based on plastic strain state produced by high residual stresses superimposed with externally applied load. The optimization process involves generating response surface equations for the LCF life and deformations and using multi-objective genetic algorithm to find the dimensions that best define the structural responses.

Chapter 2

Background

This chapter presents a brief introduction to the general additive manufacturing process and the different techniques involved in this process with a specific focus to the powder bed fusion (PBF) process. Pros and cons of PBF process being specific to selective laser melting fusion mechanism, the distortion effect caused by residual stresses on different geometries of parts and also its effect on strength and fatigue life from the perspective of previous research works are highlighted.

2.1 Additive Manufacturing

Additive manufacturing (AM) also referred to as 3D printing is defined as “process of joining materials to make objects from 3D model data, usually layer upon layer, as opposed to subtractive manufacturing methods” (ASTM, 2012). Here, 2D surfaces are stacked upon one another until the dimensions of supplied 3D CAD data is achieved for end-use application without any need for tooling as opposed to conventional means. Elimination of tooling minimizes the knowledge and skillset required by an AM user on the contrary to complex traditional manufacturing user (Gibson et al., 2015).

The process generally starts from creating a solid model of the product using a CAD software and converting it into .STL file as small triangular facets. AM also facilitates fabrication of reverse engineered data obtained by the means of 3D scanning. The STL model is then pre-processed for adjusting its orientation in the build chamber after which the regions that may require support structures can be identified. The support structures can be pre-modeled according to requirement along with the part or it may be generated automatically. After proper orientation is determined and the support structures are defined, a slicing software is used to digitally slice the model into thin cross-sections and the G-

code file is obtained which contains the coordinates for the feeding nozzle (or laser-in case of SLM process) to move around inside the build chamber to deposit (or melt) the material.

Figure 2-1 General Additive Manufacturing Process

Source: http://globaltrends.thedialogue.org/wp-content/uploads/2014/11/Could-3D-Printing-Change-the-World-Technologies-Potential-and-Implications-of-Additive-Manufacturing.pdf

Eliminating tooling, stacking up layers, etc. benefits a user in many different ways some of which are summarized as follows (Attaran, 2017) (Gibson, et al., 2015):

- Parts with any complex shape like lattice structures, internal cavities, and many other features can be fabricated.
- The amount of resources required (in terms of aerospace applications, the bye to fly ratio) is significantly reduced with AM as compared to the subtractive process.
- In some cases, the post-processing of the fabricated parts can be fully eliminated i.e. printing the parts for end use applications.
- AM enables mass customization which enables customers to get personalized product within a short period of time.

- Cost saving by on-site or on-demand manufacturing i.e. products can now be fabricated where it is needed, eliminating transportation cost.

There are a number of techniques by which the parts can be fabricated by stacking up layers for different types of material. Few of these categories are discussed briefly in the following section:

2.1.1 Additive Manufacturing Categories

VAT Photopolymerization:

In this process polymerization of photo-sensitive resin is done for solidification by irradiation with the ultraviolet light (Skoog et al., 2014). This is carried out on a base plate immersed in the resin which moves down a layer thickness repetitively until the part is built.

Material Extrusion:

This process is famous for printing thermoplastic polymers like Polylactic Acid (PLA), Acrylonitrile Butadiene Styrene (ABS), etc. Here, the polymer filaments are heated in a chamber with heating coils wrapped around to reduce the viscosity of the material. The chamber directly connects to a nozzle/extruder from which the material is extruded onto a substrate and the subsequent layers. The quality of the part fabricated from this process mainly depends on its orientation during the build, layer thickness, hatch spacing and raster pattern (Chennakesava & Narayan, 2014).

Material Jetting:

Here, the material is passed through a heated nozzle fully melting it and similar to 2D inkjet printing process, the droplets are deposited and solidified layer by layer. The accuracy of the build, its strength and stiffness characteristics, and also surface roughness are all mostly dependent on the part orientation in the build chamber (Yap, et al., 2017).

Binder Jetting:

Similar to material jetting, in this process, droplets are deposited via. a heated nozzle, however, the droplets aren't made up of the material of the actual product to be printed, instead, they are made of binders which is deposited to bind the powder particles to form a 3D model. Post processing is required to burn off the binder and sinter the powder particles together. With similitude to powder bed fusion, density of the deposited powder controls the mechanical properties of the parts fabricated with this process (Inaekyan, et al., 2016).

Powder Bed Fusion Process (PBF):

PBF is a metal 3D printing process where powder is deposited onto the substrate or previous layer through a blade or roller system and heat energy from laser or electron beam is directed onto the deposited layer either to sinter or melt the particles for fusion. Based on the type of heat energy source used, PBF process can be further categorized into Selective Laser Melting/Sintering (SLM and SLS) and Electron Beam Melting (EBM).

Although metal additive manufacturing brings about design freedom and additional design flexibility to fabricate functional structural parts with complex geometry and effective bye to fly ratio (in aerospace industry), they are severely affected in terms of geometric accuracy and strength due to built-in residual stresses and porosity. These stresses are introduced by repetitive melting and cooling process also known as subsequent thermal cycling layer by layer which causes high thermal gradient within the build (Vrancken, 2016). Consequently, it is necessary to understand the coupling effect of thermo-mechanical behavior of AM processed materials. Hence, further topics in this chapter includes residual stresses and distortions and understanding effects of these parameters as well as defects on structural response in high cycle and low cycle fatigue regimes.

2.1.2 Selective Laser Melting

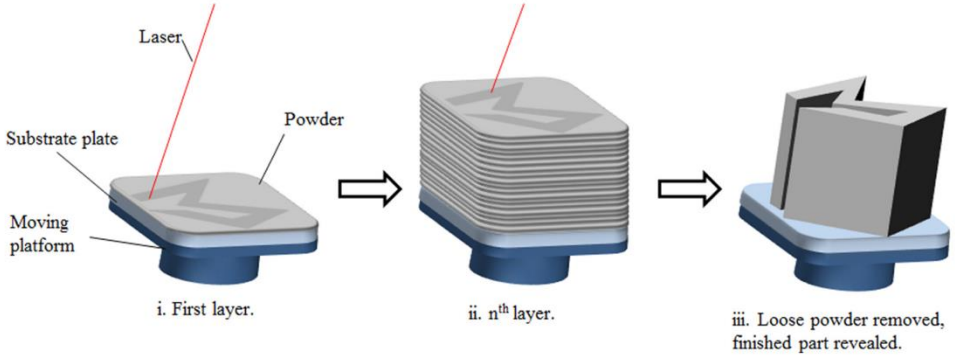

Figure 2-2 SLM process (Yap, et al., 2015)

SLM is one of the binding mechanisms in powder bed fusion process where the particles are consolidated by melting a layer and allowing it to solidify during a part build in an inert environment. The inert build chamber ensures that reactions causing the formation of metal oxides are prevented. During the build, a very thin layer of powder of about 20 to 100 μm is spread across the base plate (made of same material), the laser acts as a heat source which scans the deposited layer according to the provided coordinates. The recommended range of layer thickness provides a reasonable tradeoff between powder flowability and the resolution of the part (Yap, et al., 2015). Further, the base plate is preheated to considerably high temperature and the powder bed is maintained at a temperature just below the melting point in order to minimize thermal gradient within the part and also laser power needed to melt the deposited layer (Gibson, et al., 2015). Laser power required to melt the metal completely depends on the material being used, whereas, number of lasers/heat sources depends on the process requirement. With this technique, high density parts with comparatively good surface finish can be obtained and it also has the potential to fabricate fine/thin structures up to about 0.1 mm thickness (Wang, 2012) (Mullen, et al., 2009). The final shape and quality of the part are driven by influence of the process parameters involved in SLM technique such as laser scan speed, hatch spacing,

laser power, layer thickness, etc. that has to be addressed before any part is actually printed.

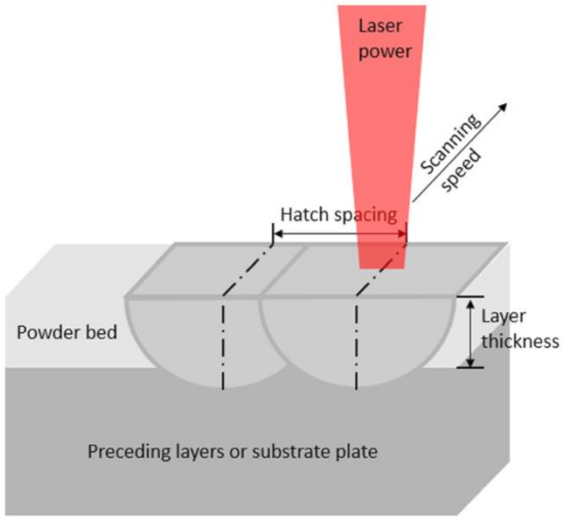

Figure 2-3 Process parameters involved in SLM (Yap, et al., 2015)

SLM Process Parameters

The parameters shown in figure 2-3 have following major categories (Gibson, et al., 2015):

- Laser power, spot size, duration and frequency
- Scan speed, spacing, and pattern
- Powder particle size, layer thickness, properties and bed density
- Temperature of the base plate, powder feeder, and the powder bed

Even though these parameters do not depend on each other, one could be influenced by another. For example, the powder bed temperature defines the heat energy required by the laser to melt the particles and size of the particles define energy absorptivity. However, among the above-mentioned parameters, the ones that are commonly modified in order to improve the quality of build are laser power, scan speed, layer thickness, temperatures

and hatch spacing (Yap, et al., 2015). Coupling large layer thickness with low laser power and high scan speed usually results in balling phenomenon caused by degradation of the wetting ability of the melt pool which is considered to be a deleterious effect to the quality of the built part (Li, J., et al., 2012). Furthermore, large hatching space causes lack of fusion between the adjacent scan which would be later retained in the part as defects, again detrimental to the quality and strength of the build. Therefore, an optimum combination of these parameters is required to ensure high density, strength and supplied CAD shape of the build. For example, Gong, et al., (2014) have studied relation between laser scan speed and laser power to achieve the build quality with greater density for Ti-6Al-4V.

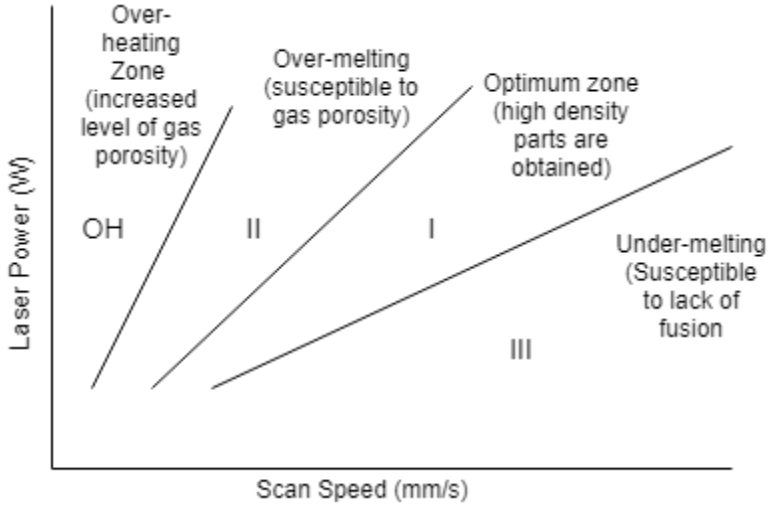

Figure 2-4 Relation between two SLM process parameters (Laser Power Vs Scan Speed) to achieve high density parts (Gong, et al., 2014)

Here, zone I is the optimum zone where full density parts were achieved whereas, zone II and III are accounted for over-melting and under-melting respectively, both resulting in copious porosity in the build either in gaseous form or due to lack of fusion. OH is the overheated zone which only aids to amplify the defect density by influencing gas porosity.

2.2 Residual Stress

Residual stresses are the stresses retained by a solid body after external or in-service loads on the part have been removed and equilibrium state is achieved (Mercelis & Kruth, 2006). Externally applied load could take forms as thermal gradient, fluid pressure, force, moments, etc. which are resisted by a structural component. When a metallic load bearing structure is subjected to any of these loads that may cause nonuniform plastic deformation, some part of the stresses would remain inside the material as residual stresses (Vrancken, 2016). These stresses are not only limited to metals but could also be present in all kinds of solid bodies like polymers, composites, wooden ply, etc. The primary source of cause of residual stresses in metals could be directly correlated with the process parameters used in manufacturing techniques. For example, in welding, when two metallic parts are melted locally to form a single welded joint, the heat generated in the melt pool would be sufficient enough to cause inhomogeneous plastic deformation at elevated temperature due to local softening which in turn results in high localized residual stresses (Leggatt, 2008). They have not ever been disadvantageous, for example, compressive stresses introduced at the surface of a metal via. Shot Peening (a cold working process) would cause plastic deformations, however, it strengthens the part and also increases fatigue crack propagation life (Miao, Demers, Larose, Perron, & Lévesque, 2010). Another example could be frequent high cooling rates imposed on glass plates which can induce compressive stresses at the surface of the plates which increases resistance to load preventing crack propagation (Mercelis & Kruth, 2006).

In general, residual stresses can also be understood in terms of scale of self-equilibrating length (Vrancken, 2016). $Type\ I$ residual stress occurs in a macroscale and it distributes itself across an entire part causing large amount of deformations. Further, $Type\ II$ is one of the microscale residual stresses which occurs over a few number of grains

and is ubiquitous in almost all polycrystalline materials. Finally, $Type\ III$ residual stresses are defined over even smaller scale and may occur within a single grain in a crystalline structure in the form of defects like dislocations and vacancies.

In additive manufacturing, the primary source of cause of these stresses is the presence of high thermal gradient throughout the part during its build. According to Mercelis & Kruth (2006), in the SLM process, residual stresses induce in the part with two mechanisms:

1) When the laser melts the powder deposited at the top layer of the part, the expansion of the melt pool would be resisted by material underneath which causes compressive stresses to be induced in the layer. In extreme temperatures, the yield stress of the metal decreases, causing the induced stresses to produce plastic deformations.
2) During cooldown phase of the material, shrinkage occurs which also affects previously deposited material underneath the layer. This results in tensile residual stress at the top layer, whereas, compressive at the bottom.

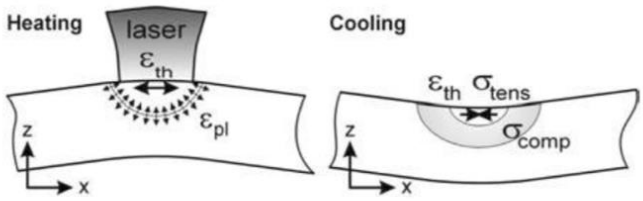

Figure 2-5 Stresses during heating and cooling in SLM (Mercelis & Kruth, 2006)

In a temperature gradient environment, the induced stresses can be represented with following equation:

$$\sigma(T) = E(T) * \alpha_{CTE}(T) * (T_m - T)$$ (Vrancken, 2016)

It is important to notice that $E(T)$ and $\alpha(T)$ are temperature dependent and these parameters along with T_m are material specific properties. Hence, the only controllable parameter in the above equation is T which could either be the preheat temperature of the base plate or the powder bed temperature. In SLM process this may not be enough to completely define the stress state since there are other parameters which could entirely depend on user input like scan speed, layer thickness, etc. proven to have influence on the residual stress. However, the residual stress is also bounded by melting temperature of the material which cannot be user defined. Higher melting temperature in combination with low powder bed and preheat temperature causes larger thermal gradient and hence larger stresses and vice versa.

Stresses accumulate in the part anchored at the base plate until the final layer is fused with the underlying material and they are retained in the part even after the system cools down to the room temperature. Cutting off the part from the baseplate significantly reduces these stresses due to relaxation and the stresses are relaxed even more after removal of the support structures (if present). This phenomenon results in a very noticeable deformation of the part as shrinkage and bending (Mercelis & Kruth, 2006). Many approaches have been experimented and simulated in order to mitigate these stresses. Xing, et al. (2018), have shown that in an amorphous alloy, cross scanning of laser between the longitudinal and transverse direction along with preheating of the base plate facilitates homogeneous shrinkage in all directions throughout the part (Xing, et al., 2018). This often results in relatively low residual stresses when compared to conventional scanning method. On the other hand, increasing number of layers tend to increase the stresses since the gradient field is increased. Mercelis & Kruth (2006), have shown that residual stress is also a material dependent property as materials with higher yield stress have more influence on the residual stress as illustrated by figure 2-6.

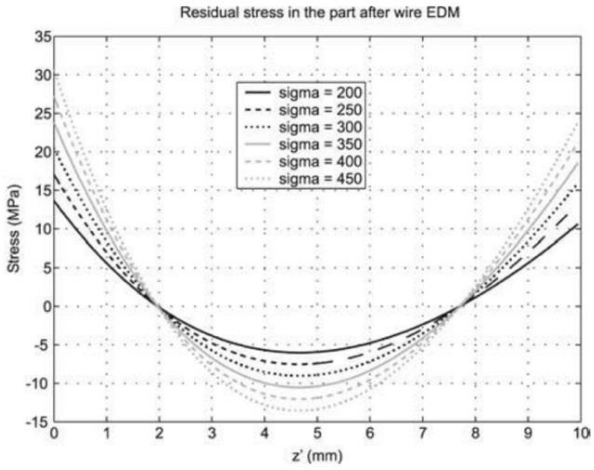

Figure 2-6 Effect of material's yield stress on residual stress profile (Mercelis & Kruth, 2006)

2.2.1 Measurement of Residual Stresses and Distortion

Distortion Mapping

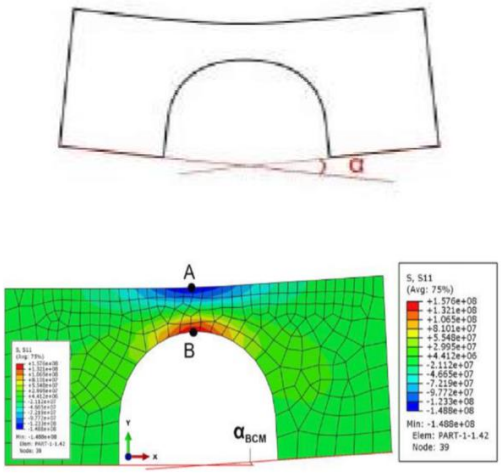

Figure 2-7 Applying angle between cut planes as a boundary condition in FE model (Vrancken, 2016)

There has been an immense amount of research ongoing to predict the residual stresses and the deformations in different geometries which could be features defined

within a complex component to be printed. Majority of the works have relied on an indirect approach to measure strains or displacements that occur when the stresses redistribute themselves after the material is allowed to deform (Masubuchi, 2013) (Ekmekçi, et al., 2004). Vrancken (2016) used bridge curvature method (BCM) by measuring angle between two cut planes of a bridge shaped specimen and applying it as a boundary condition in a stress-free Finite Element model as shown in figure 2-7. This predicts the magnitude of residual stresses in the model with poor accuracy as the stresses were concentrated only around the thin overhang of the specimen. Hence, mapping the end displacements would not be very reliable to produce the actual state of the stresses in the model.

Other geometric features like cantilever overhang, T-shaped cantilever overhang, etc. are also extensively used specifically to analyze distortion mechanism under variation of process parameters of SLM. Buchbinder, et al. (2014) studied distortion behavior of SLM fabricated T-shaped specimen with different thicknesses made of AlSi10Mg alloy, with and without preheated condition of the baseplate. It was shown that with preheating, the distortions can be reduced significantly along with formation of cracks in the components as the thermal gradient is lowered which consequently lowers the thermal stresses (Buchbinder, et al., 2014).

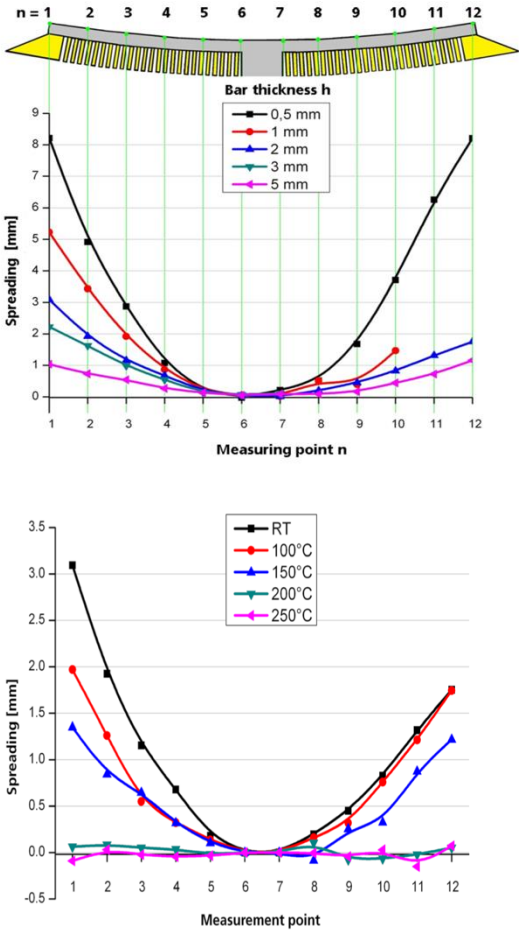

Figure 2-8 Deflection measured without preheated substrate (top); Effect of preheating substrate at different temperatures on 2mm thickness specimen (bottom)

It has been assumed that yield stress acts as an upper limit to residual stress i.e. final stress state retained by the SLM fabricated component, after it has cooled down to room temperature is claimed to be always less than yield stress of the material (Vrancken, 2016) (Mercelis & Kruth, 2006). However, Zaeh, et al. (2010) have reported higher than yield Von Mises stress from FEM simulation in small localized regions of their specimen. This could be largely attributed to the fact that residual stress in SLM mostly depends on the strains ($\alpha\Delta T$) casued by the differential temperature (ΔT), hence, stresses may take

magnitude higher than yield depending on this parameter solely if other process parameters are assumed to be constant.

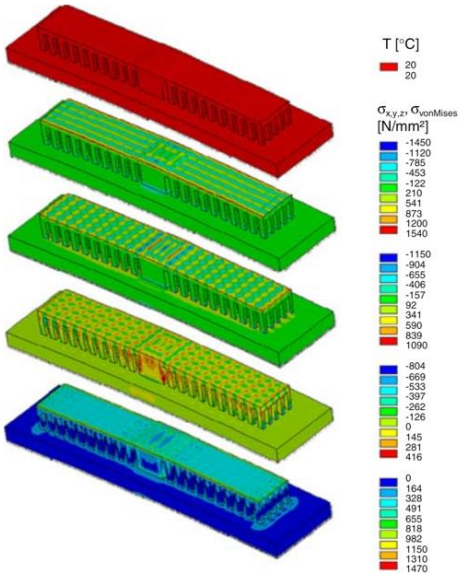

Figure 2-9 Stresses showing higher than yield Von Mises stress in Ti-6Al-4V (Zaeh & Branner, 2010)

X-Ray Diffraction (XRD)

This is a non-destructive process of residual stress measurement where a regional area of a component is exposed to X-Ray. Depending upon the absorption coefficient of the material for X-Ray, the beam penetrates to a certain depth and gets diffracted giving an estimation of strains in crystal lattice (Prevey, 1986).

Contour Method

Here, the component with certain level of residual stress state is cut in two pieces which causes the perpendicular stresses to relax, hence, causing deformations. With the deformation data from the plane of the cut surface, the original residual stress state can be calculated precisely (Prime, 2009). The way this is done is by forcing the deformed geometry to match the pre-relaxed geometry i.e. the stress state of the deformed geometry

would be superimposed with applied stress in order to get a sense of the magnitude of the original residual stress (Pagliaro, et al., 2008). It should be noted that using this method would only enable to estimate stresses in the cut plane and not throughout the entire part.

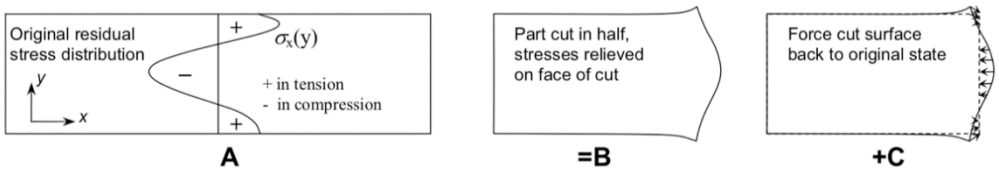

Figure 2-10 Contour method of predicting residual stresses (Pagliaro, et al., 2008)

Layer Removal Technique

This is very much similar to contour method and the only difference lies with the fact that in this method, small slices of a number of layers are cut off from the part instead of cutting the part in only two pieces. Assumptions made here are similar to contour method which follows:

- The relaxation deformation is elastic.
- There are no external stresses imposed during slicing process.

The residual stress state throughout the thickness of the part can be estimated with this process. Strain gauges are placed at the very bottom of the part and layers are cut off from above (Greving, et al., 1994). Voltage readings are taken from the strain gauge during each slice which can be easily be converted to strain and thus stress values with relational equations (Levkulich, 2017).

Protasov, et al. (2016) used this approach to study residual stress profile by cutting off SLM fabricated beam with square cross-section made up of stainless steel into thin plates and measuring the deformations of the cut-off plates. This deformation data was fed into stress-displacement equation for estimation of the induced stresses in the original part.

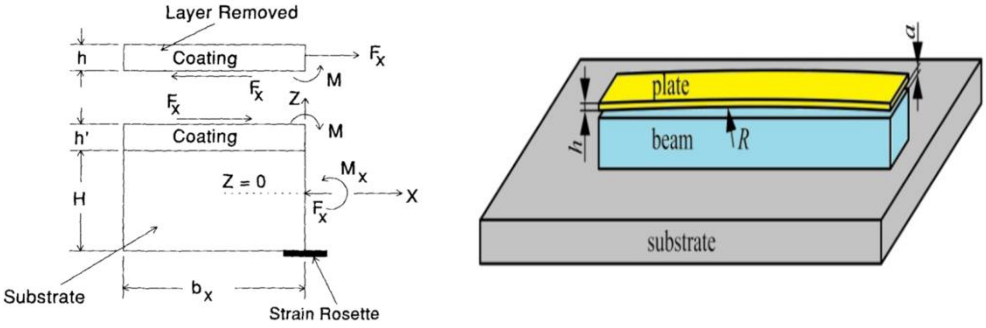

Figure 2-11 Layer removal mechanism (Left) (Greving, et al.,1994); Model used to predict the stresses (right) (Protasov, et al., 2016)

2.2.2 Effect of Residual Stresses in Structural Response

The effect of residual stress in context of structural components can be summarized as following:

- As it was discussed in the previous sections, large unwanted deformations can be seen in the SLM fabricated components due to self-equilibrating nature of the induced stresses.
- These stresses tend to superimpose with the externally applied stress and the net stress state will essentially be algebraic sum of the two. This may cause unexpected failure of the material in static and cyclic loading.
- $Type\ I$ and $Type\ II$ tensile stresses if present in within a component, may cause stress-corrosion. As these stresses tend to act in the grain boundaries, it may result in intergranular stress-corrosion cracking (Withers, Residual stress and its role in failure, 2007) (Dieter & Bacon, 1986).

2.3 Fatigue in metal additive manufacturing

The static strength (tensile and compressive strength, hardness, etc.) of the parts fabricated with metal AM process are very much comparable to their traditional forms (Bian, et al., 2015). However, there has been a major issue reported in the literature regarding

the response of the structural AM components to its durability in cyclic loading. Fatigue is one of the common and most unpredictable mode of failure that occurs in structural components. In metal SLM parts, this phenomenon of failure is mostly affected by porosity due to lack of fusion, induced residual stresses due to large thermal gradients, microstructural behavior inflicted by high cooling rates during the build and surface roughness.

2.3.1 Fatigue Crack Growth Rate

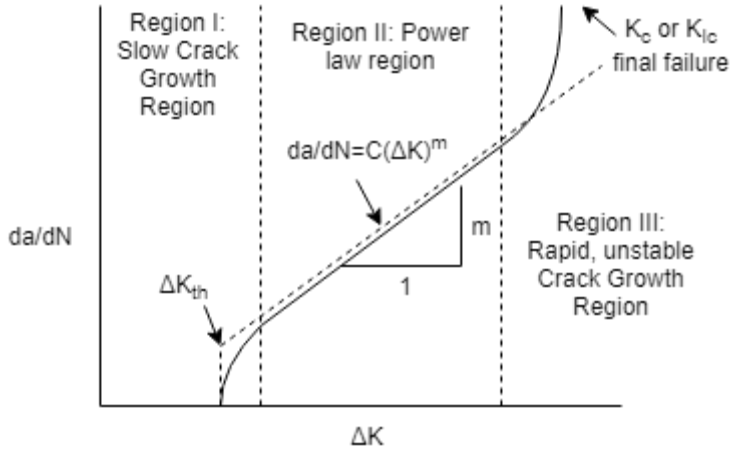

Figure 2-12 Fatigue crack growth curve (log scale) (Ambriz & Jaramillo, 2014)

To understand the effect of residual stresses on fatigue crack growth rate, let us consider FCGR curve as shown in figure 2-12. The first region is non-linear where ΔK (the change in stress intensity factor) is less than its threshold ΔK_{th} for a crack to propagate. Second region in the curve is linear and it follows the equation $\frac{da}{dN} = C(\Delta K)^m$ where da/dN is the crack growth rate, C and m are the material constants. Crack propagation is again nonlinear and unstable around ΔK_{max} in the third region. Although this curve addresses critical parameters like size of defects, applied stress, etc., it does not convey the information of mean stress and stress ratio ($R = \frac{\sigma_{min}}{\sigma_{max}}$) on crack growth (Vrancken, 2016).

Since, ΔK is the difference between its maximum and minimum values, the superimposed residual stress has no effect on it and hence, no effect on the linear region of the curve.

$$\Delta K = K_{max} + K_{res} - (K_{min} + K_{res}) = K_{max} - K_{min}$$

Despite of this, the mean stress does change by the superposition and hence the stress ratio to $R = \frac{K_{min}+K_{res}}{K_{max}+K_{res}}$ (Webster & Ezeilo, 2001). This change has been reported to significantly influence the first and third regions of the curve i.e. the regions with stress intensity factor at the threshold and peaks (Withers & Bhadeshia, 2001).

2.3.2 Low Cycle Fatigue

Low cycle fatigue regime is driven by the strains and stresses originating in localized plastic regions which are usually highly stressed geometric features susceptible to crack initiation (Roberts, 2002). This fatigue regime is sensitive to plastic strain amplitude or ductility of the material, as an increase in the amplitude decreases the fatigue life and vice versa. It has been reported in the literature that residual stresses have small to no influence in the low cycle fatigue regime because after the initial cycles, when the applied load causes considerable amount of plastic deformation, previously induced stresses are said to be washed out (Vrancken,2016) (Gharizadeh, et al., 2013). Nevertheless, it should also be noted that for a given magnitude of load in the absence of residual stresses, a structure may perform well within elastic region which might not reflect upon the case when the component is pre-stressed or pre-strained. To further elaborate this effect, if the initial strains are high enough such that the applied load produces localized plastic strains, the fatigue regime may shift from high cycle to low cycle, therefore, substantially degrading the total number of cycles a component could withstand before failure. This phenomenon can be explained with Basquin and Coffin Manson's curves which are derived from stable cyclic stress-strain curve obtained from strain controlled fatigue test.

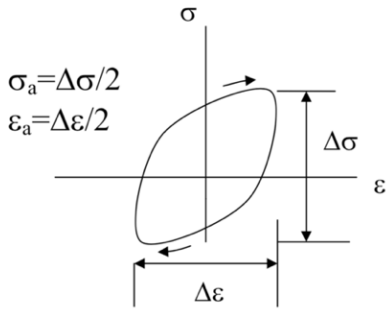

Figure 2-13 Schematic of cyclic stress-strain curve

Figure 2-13 shows the cyclic stress strain curve obtained by loading, unloading and reverse loading process in a uniaxial fatigue test. The total strain amplitude shown in the curve is given by,

$$\varepsilon_a = \varepsilon_e + \varepsilon_p = \frac{\sigma_a}{E} + \left(\frac{\sigma_a}{H'}\right)^{\frac{1}{n'}} \qquad (2.3.1)$$

Where $H'$and n' are curve fitting constant and ε_e and ε_p are elastic and plastic strain amplitude respectively.

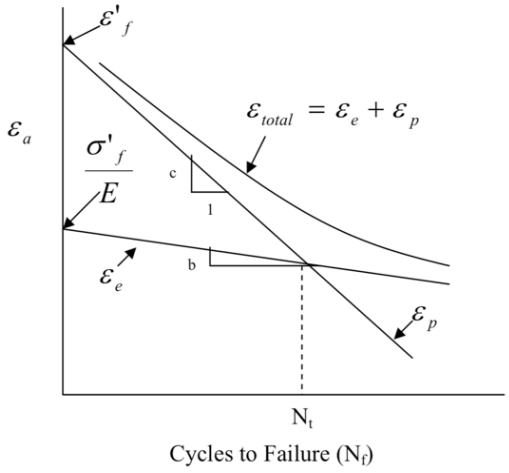

Figure 2-14 Strain-life curve

Figure 2-14 shows Basquin and Coffin Manson's curve, which signifies total number of strain cycles before failure in log scale. The two linear curves represent elastic and plastic strains and the point where these intersect is the transition point from low cycle to high cycle fatigue.

The two terms from equation (2.7.1) can be written as,

$$\varepsilon_e = \frac{\sigma_a}{E} = \frac{\sigma_f'}{E}\left(2N_f\right)^b \quad (2.3.2)$$

$$\varepsilon_p = \varepsilon_f'\left(2N_f\right)^c \quad (2.3.3)$$

Equation (2.7.2) is the Basquin relationship for elastic strain amplitude with fatigue life. This equation is predominantly driven by strength of the material in elastic region pertaining to high cycle fatigue. Equation (2.7.3) is known as the Coffin-Manson's equation driven by plastic strains in low cycle regime. These equations will be used later in the report to evaluate the effect of residual strains in fatigue life of the specimens.

2.3.3 Critical Factors Affecting Fatigue Life

Different processes and parameters that have sensitivity to fatigue life of a component are discussed further from the perspective of previous studies. Fatigue crack growth properties and microstructural behavior on SLM processed Maraging Steel (MS) 300 alloy have been studied by Suryawanshi, et al. (2017). The tests were performed on the specimens in as-built as well as aged condition. Even though the SLM processed alloy and conventionally manufactured (CM) alloy, both were treated with aging heat treatment, they had significant microstructural differences. Nevertheless, the evaluated mechanical properties of the 3D printed alloy were found to be very close to the data available for aged CM MS 300 which could be attributed to the effect of austenite-martensite transformation along with residual stress relaxation during aging heat treatment (Suryawanshi, et al., 2017). Despite of the fact that post-processing would be counterproductive to what AM

offers (i.e. end-use part fabrication), it can be concluded that heat treatment such as annealing, aging, etc. maybe beneficial to improve mechanical properties of the SLM fabricated part.

Analyzing the study on Ti-6Al- 4V in as-built condition by Edwards, et al. (2014) showed that fatigue life in high cycle regime was 75% lower than the wrought material which was reported to be due to poor surface finish, presence of porosity and the tensile residual stresses being superimposed with the applied remote loading. This degradation is very substantial and thus suggests the necessity of post processing procedures

In general, the HCF tests are performed dominantly within elastic region of deformation and thus stress data with respect to number of cycles to failure provides reasonably sufficient information for predicting the behavior. In contrast, fatigue behavior in the low cycle regime can be evaluated only if the stress is high enough to cause plastic deformation after which the accounting of loading in terms of stress would be less useful and the value of strain the material is subjected to offers simpler and more accurate analysis on the fatigue behavior. Following this theory, LCF life for as-built specimen condition was predicted for SLM manufactured biomedical titanium grade 23 by Benedetti et al. (2018), where significant softening was reported for cyclic loading which is very unlikely for the chosen alloy. The detrimental effect could be attributed to surface cracks that hadn't been removed prior testing.

While residual stresses and porosity are crucial factors in determining the fatigue life, surface roughness is also decisive. According to the theory of 'Linear Elastic Fracture Mechanics' (LEFM) which conveys that surface cracks tend to propagate more rapidly than the embedded ones because the stress intensity factor 'K' of former is 1.12 times greater than the latter (Anderson, 2017). Although this factor was attempted to be accounted by Edwards and Ramulu (2014) for its effect in fatigue life, presence of residual stresses and

embedded porosity created ambiguity in the obtained data. Therefore, their effect must be eliminated using post-processing procedures (such as annealing and HIP) in order to establish an understanding of influence of surface roughness on fatigue life.

Additionally, porosity affects void growth increasing strain localization between the voids, causing necking between them and their coalescence for fracture to occur which is explained by Anderson (2017). This can only be minimized if the part formed is dense enough and the properties are near to isotropic in nature. One of the means of forming a denser part is through a heat treatment process known as Hot Isostatic Pressing (HIP) where the parts are subjected to high temperature along with an external pressure. In fact, Wu et.al (2017) investigated the effect of hot isostatic pressing on fatigue property of the alloy Ti-6Al-4V produced using selective laser melting where it was found that fatigue strength as well as fatigue endurance ratio in high cycle regime markedly improved with HIP due to formation of a denser part and tougher $\alpha + \beta$ phase microstructure which would cause crack blunting, thus reducing the stress concentration around the crack tip and ultimately mitigating the propagation rate.

Characterization of fatigue behavior is also critical to the geometry of the specimen to be used. ASTM E606/E606M – prescribes set of specimens which can be used in strain-controlled fatigue testing. The flat specimens tend to possess more stress concentration in the corners and hence may cause unpredicted effect during the experiment, whereas, the cylindrical specimen have no corners in the gauge section, thus eliminating the ambiguity (ASTM E606/E606M-12, 2012). Subsequently, problem that should also be addressed during fully reversed test is the effect of buckling on the specimen used as this would impose another mode of failure in the specimen which inflicts an error in the obtained data. In the context of this issue, Sandhya et al. (1994) have studied the variations of results obtained in different cylindrical specimen one of which was hourglass gauge section and

two were with uniform gauge section having length to diameter ratio of gauge section (L/D) of 5 and 2.5. The problem addressed is buckling during compression phase of the fully reversed test which showed a noticeable effect on the fatigue life of specimen with L/D of 5. Despite hourglass cross-section specimen had minimum effect of buckling amongst the three, it has been reported that data obtained could not be relied upon completely because the volume of the material acted upon by maximum stress would be very small, consequently limiting the prediction of diametral strain which relates to plastic deformation in the gauge section. Nevertheless, specimen with L/D ratio of 2.5 is reported to have adequate volume under maximum stress and less prone to buckling.

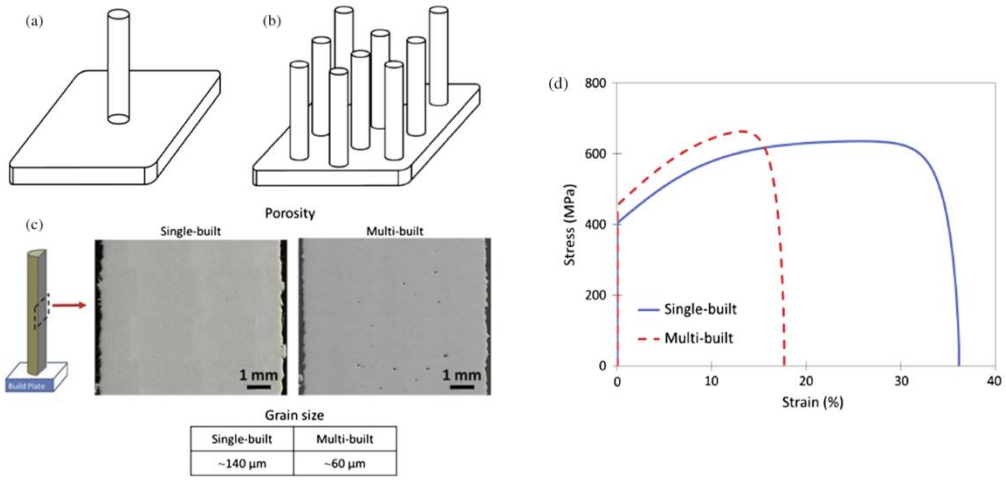

Figure 2-15 Difference between (a) single built and (b) multi-built in terms of (c) porosity distribution and (d) stress-strain curve (Yadollahi & Shamsaei, 2017)

The mechanical testing data collected from all these experiments may be unreliable to be considered as actual representation of the part made up of same material (Yadollahi & Shamsaei, 2017). This occurs due to difference in thermal history experienced by the part and the specimen. Since the size and geometry is different, the dwell time i.e. the time interval involved from moving one layer to another will be different for each case which causes different cooling rates and hence, different thermal history (Yadollahi, et al.,

2015). This difference in cooling rate would cause variation in microstructures as high cooling rates imposed in each layer have the effect of finer microstructure, nevertheless, it increases residual stresses significantly. Not only part geometry but also variation in number of parts fabricated in a single build plate and their orientation plays an important role in determining the inter-layer time during the build (Yadollahi & Shamsaei, 2017).

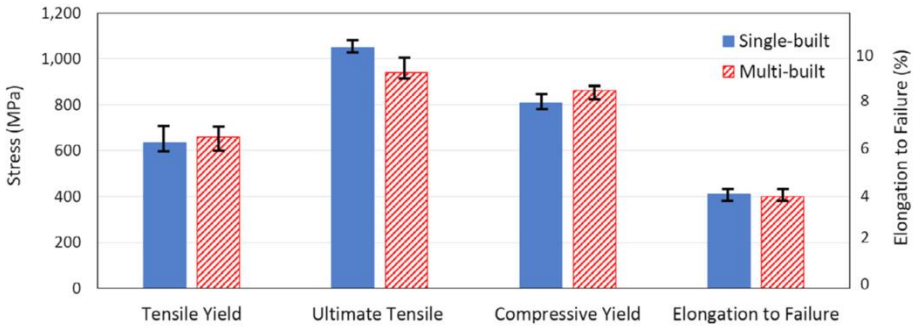

Figure 2-16 Difference between tensile yield, ultimate tensile, compressive yield and elongation to failure in single-built Vs multi-built (Mahmoudi, et al., 2017)

Another important factor that affects the crack propagation rate is the orientation of the part inside the build chamber. Its effect on the stress-strain curve and strain life have been illustrated in figure 2-17, where the data obtained for horizontally built part is compared with vertical build. This also changes the orientation of the induced anomaly and thus induces anisotropy in the part which results in different values of static and cyclic strength properties of the material in different orientations (Yadollahi, et al., 2017) (Kobryn & Semiatin, 2001). It has been observed and reported that parts built horizontally i.e. with fewer number of layers tend to possess higher fatigue resistance along with better static properties than parts built vertically or with a greater number of layers (Shrestha, et al., 2016).

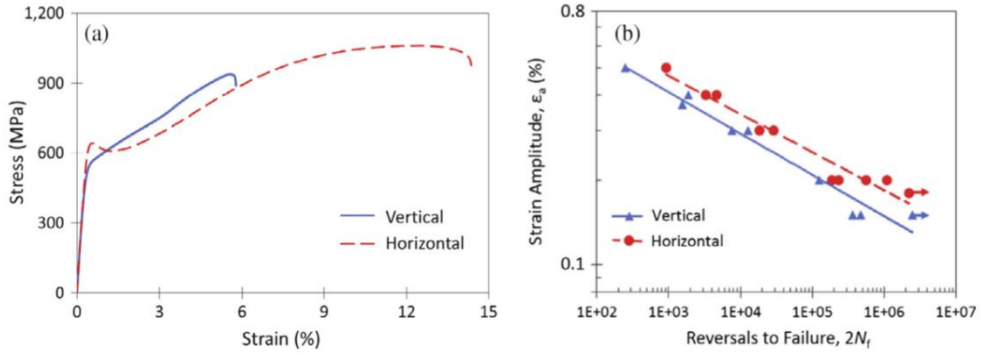

Figure 2-17 Stress-Strain curve (left) and Strain-life curve (right) for Horizontal build Vs Vertical build (Yadollahi, et al., 2017)

2.4 Design of Experiments (DOE)

Since the research is mostly related to shape optimization of a 3D printed structure using design of experiments, it is important that reader should have knowledge of some of its basic features. Hence, this section is completely dedicated to introducing the reader to DOE, the factorial design used in the current work and also the response surface tool.

Design of experiments is a method to analyze the effect of input parameters on the output/response of a process in a system. It is a tool that gives the user a sense of the effect of variation of one single factor holding all the other factors as constants and also the effect of combination of two or more factors at several number of steps or levels, thus removing the influence of superfluous parameters on the response of the system (Stat 503, Design of Experiments, 2018).

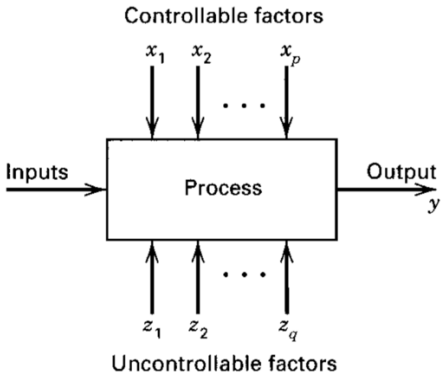

Figure 2-18 General process model of a system (Montgomery, 2017)

As it can be visualized in the figure 2-18, a system maybe composed of controllable and uncontrollable factors and other possible inputs which may represent machine, people, chemical concentration, temperature, dimensions, etc., the combination of which produces the system output with multiple noticeable feedbacks which can be very advantageous in the following ways (Montgomery, 2017):

- The most sensitive factor affecting the outcome can be identified.
- The range of factors that produces desirable response with minimum tolerance can be established.
- A point of combination of controllable factors which generates a response with minimal effect of uncontrollable parameters can be identified.

2.4.1 Factorial Design

This design is mostly suitable for the study of experiment involving two or more factors. This is done by analyzing all the sets of potential combination of factors in each run of the experiment. For example, if there are x factors of A and y factors of B, then in factorial design of experiments, each trial is influenced by the combination of xy together.

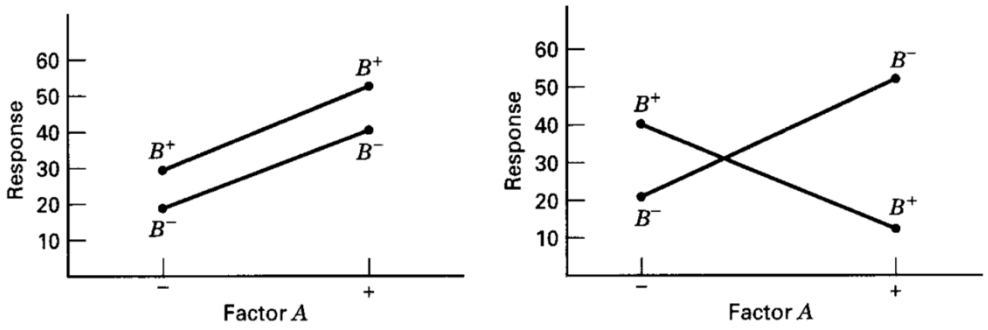

Figure 2-19 Factorial experiment without interaction (left) and with interaction (right) (Montgomery, 2017)

Influence of a factor can be seen as it causes change in response in different levels which is generally termed as 'main effect' (Montgomery, 2017). In some cases, the level of one factor might not be same throughout the levels of other factors which is said to be a cause of an 'interaction' between them as shown in figure 2-19. If we consider 2 factors 3 levels design of experiment, the approximation function with all the quadratic terms for the regression model could be written as,

$$F(x_1, x_2) = a_0 + a_1x_1 + a_2x_2 + a_3x_1^2 + a_4x_2^2 + a_5x_1x_2 + \varepsilon$$

Here, $F(x_1, x_2)$ is the response, x_1 and x_2 are the factors each at three levels and ε is the error of approximation. Here, the term with variable x_1x_2 denotes interaction between them whereas, other terms are either constant or with independent effect on the response.

3^2 *factorial design*

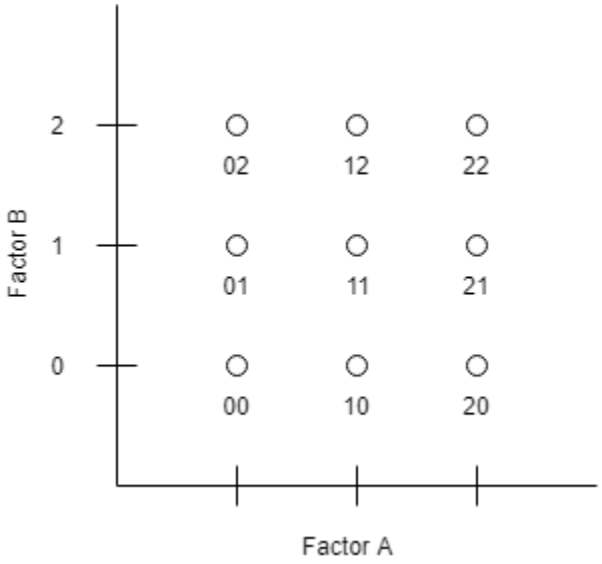

Figure 2-20 3^2 Design schematics

Derived from: https://www.itl.nist.gov/div898/handbook/pri/section3/pri339.htm

In this method there are a total of two factors each assigned with 3 levels and are generally considered as low, medium and high levels denoted by 0,1 and 2 respectively. The third level in the design helps creating quadratic relationship between the response and the factors (independent variables) in the regression model. The quadratic equation thus facilitates in creating curvature of the response surface making it more accurate for actual representation of the data.

The regression model that can be fitted for this design is,

$$F(x_1, x_2) = a_0 + a_1x_1 + a_2x_2 + a_3x_1^2 + a_4x_2^2 + a_5x_1x_2 + \varepsilon$$

Determining the coefficients $a_0 \dots a_5$ will be later shown in the section 3.2.

2.5 Response Surface Methodology

Response surface method (RSM) is a tool used for design and analysis of a process which operates using statistical data and mathematical equations in order to

achieve the goal of optimization or response of the system (Oehlert, 2000). The response surface mostly operates using equations from regression fit of the statistical data obtained from the experiment. Subsequently, it has the ability to optimize not only single response but multiple responses by analyzing and iterating all the possible outcomes from the given factors and finding the compromised optimum (Oehlert, 2000). Furthermore, this method facilitates to achieve optimization with the consideration of constraints that govern the system. Graphical representation of the response surface can be visualized below:

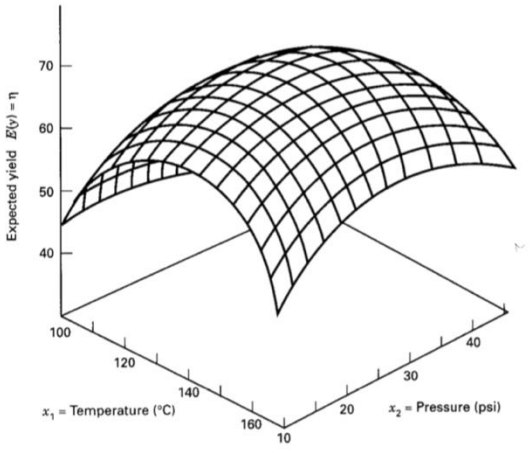

Figure 2-21 Graphical representation of a response surface consisting of two independent variables in x and y with its response in z (Montgomery, 2017)

In RSM, first a suitable approximation equation should be selected that can represent a true working relationship between the independent variables and the response (Montgomery, 2017). The equation is mostly modeled using either first order linear or second order quadratic approximations as shown below:

$$f(x_1,..x_n) = a_0 + a_1x_1 + a_2x_2 + \cdots a_nx_n + \epsilon \qquad (2.5.1)$$

This is a first order equation and shape of the surface it generates is essentially linear with no curvatures. The second order approximation creates curvature and may take the following form:

$$f(x_1, x_2) = a_0 + a_1x_1 + a_2x_2 + a_3x_1^2 + a_4x_2^2 + a_5x_1x_2 + \epsilon \quad (2.5.2)$$

We may employ linear regression to find the coefficients of the above equations. Montgomery (2017) has discussed this process in following way:

Using the assumptions,

$x_3 = x_1^2;\ x_4 = x_2^2;\ x_5 = x_1x_2$, we get,

$$y = f(x_1, x_2) = a_0 + a_1x_1 + a_2x_2 + a_3x_3 + a_4x_4 + a_5x_5 + \epsilon \quad (2.5.3)$$

Writing equation (3.2.3) in its general form as,

$$y_i = a_0 + a_1x_{i1} + a_2x_{i2} + \cdots + a_nx_{ik} + \epsilon_i$$

$$= a_0 + \sum_{j=1}^{k} a_jx_{ij} + \epsilon_i$$

Writing this in matrix form

$$y = Xa + \epsilon \quad (2.5.4)$$

Using method of least squares which employs sum of square of error to be minimized,

$$S = \sum_{i=1}^{n} \epsilon_i^2$$

$$= \sum_{i=1}^{n} \left(y_i - a_0 - \sum_{j=1}^{k} a_jx_{ij} \right)^2$$

S can be written as,

$$S = \epsilon'\epsilon = (y - Xa)'(y - Xa)$$

Where y is $(n \times 1)$ vector, X is $(n \times p)$ matrix with $p = k + 1$ and a is $(p \times 1)$ vector.

S can also be written as,

$$S = y'y - 2a'X'y + a'X'Xa \quad (2.5.5)$$

Now, the equation of S has to be minimized with respect to $a_0, a_1, \ldots, a_k$.

$$\left(\frac{\partial S}{\partial a}\right)_{\hat{a}} = -2X'y + 2X'X\hat{a} = 0$$

Simplifying to,

$$\hat{a} = (X'X)^{-1}X'y \qquad (2.5.6)$$

Hence, the fitted new equation of the response surface can be written as,

$$\boxed{\hat{y} = X\hat{a}} \qquad (2.5.7)$$

And the residual is given by $e = y - \hat{y}$

Equation (2.5.7) is used to generate the equation of response surfaces further in this report while equation (2.5.6) is used to calculate the unknown coefficients of the approximation.

Chapter 3

Methodology

3.1 Overall Process of Design Optimization

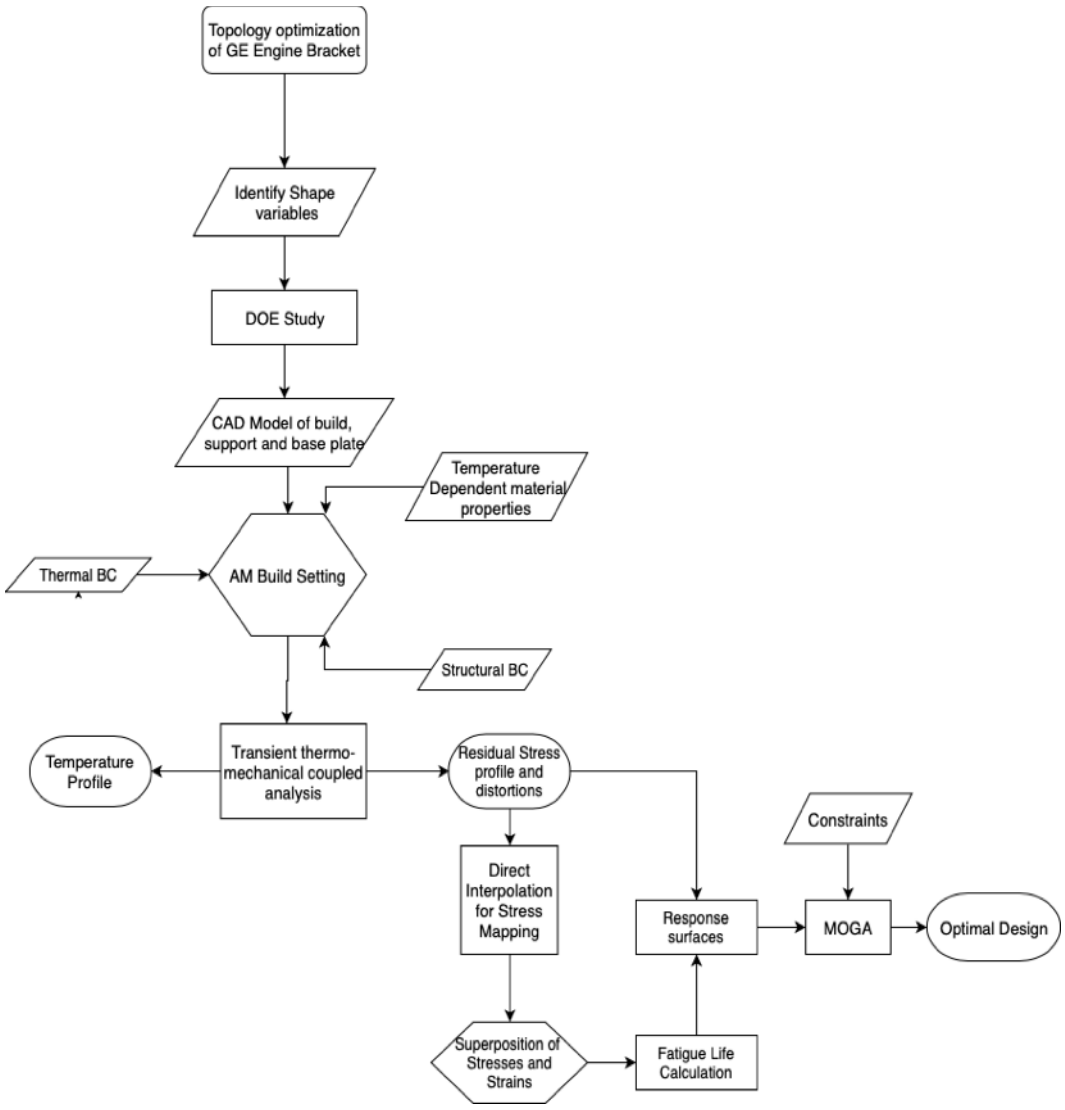

Figure 3-1 Flowchart summarizing the design optimization process

Current work provides a framework for structural optimization for components fabricated with selective laser melting process with consideration of fatigue life and distortion which is affected by process induced residual stresses. This is achieved by

generating response surfaces that relates the geometric features to its fatigue life and distortion and using the equations of the obtained surfaces as constraints in shape optimization of the structure. This chapter is completely dedicated to vivifying the reader about following points:

- Inspiration for the selected shape of the structure
- Factors selected for the DOE study and their assignment
- The properties of the material that are to be defined in additive simulation process
- SLM process parameters
- Mapping process of stress result among dissimilar meshes with direct interpolation
- Response surface optimization algorithm

3.2 Topology Optimization of Jet Engine Bracket

The shape of the structure selected for the study is mostly a fit-in model to shape obtained from topology optimization process of an engine bracket. To elaborate this with some detail, the loading bracket of GE jet engine was considered which is shown in figure 3-2.

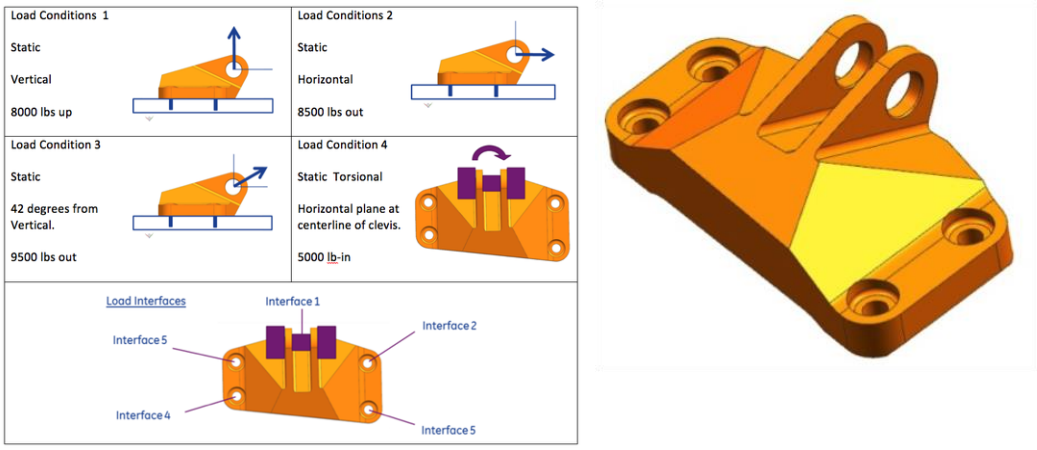

Figure 3-2 Loading cases of GE engine bracket

The loading cases here are as follows (GE jet engine bracket challenge, 2013):

- Static load of 8000 lbs vertically up,
- Static load of 8500 lbs horizontally out,
- Static load of 9500 lbs 42 degrees from the vertical
- Static torsional load of 5000 lb-in acting on horizontal plane at centerline of clevis

The optimization was carried out in Altair's OptiStruct solver with constraints of 20mm on minimum and 40mm on maximum member size. Additionally, noisy optimization result was smoothened with Polynurbs tool in solidThinking Inspire using elements with densities greater than 50%. Consequently, the weight of the structure was reduced to almost 60% of the original part. The result of the optimization is shown in figure 3-3.

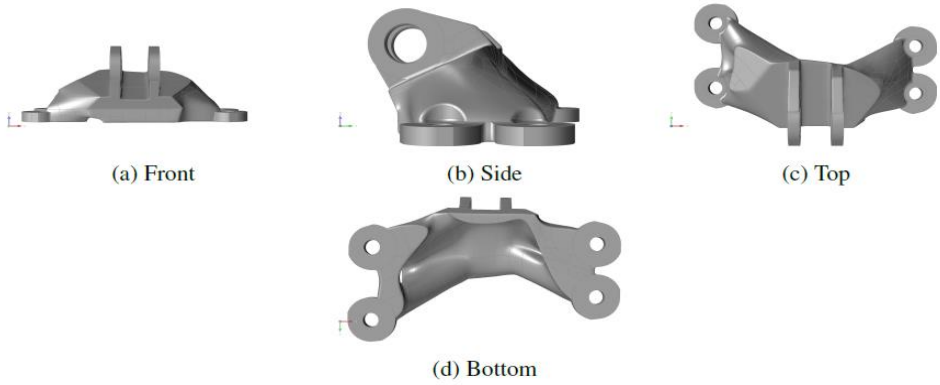

Figure 3-3 Topology optimization result of the engine bracket; max. member size: 40mm, min. member size: 20mm [to be published by Chahal & Taylor (2019)]

The cross-sectional images of the front view of the above result is illustrated in figure 3-4. These images reveal symmetry to an overhang bridge shaped structure due to which such structure is considered in the further study.

Figure 3-4 Images of the cross-sections through the part from the front view [to be published by Chahal and Taylor (2019)]

The stress analysis on the model shown above reveals that the design is still considerably conservative which makes the current study ideal for further shape optimization.

3.3 Factors of Overhang Bridge for DOE Study

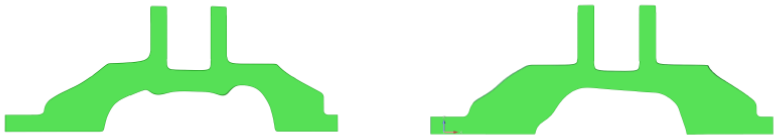

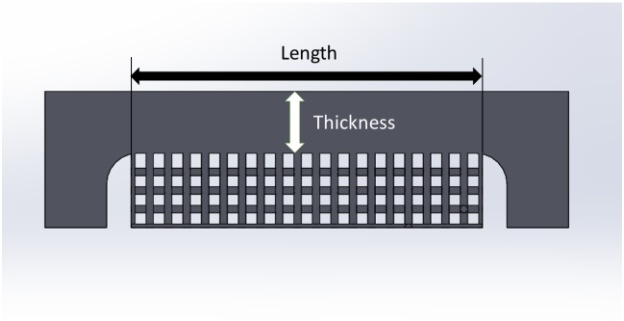

Figure 3-5 Factors of DOE study

3.3.1 Length of Overhang

It has been reported that length of the overhang portion of 3D printed components has a direct effect on the distortion (Buchbinder, et al., 2014) (Vrancken, 2016). Overhangs with greater length tend to show higher deformations and hence, this effect is necessary

to be comprehended. Three levels of length selected for the study are 35mm, 50mm and 65mm.

3.3.2 Thickness of Overhang

Increasing thickness of the feature tends to increase the number of layers for the part to be printed consequently affecting the thermal gradient field and hence the residual stresses mostly in the build direction. Three levels taken for this factor are 5mm, 7.5mm and 10mm.

Table 3-1 Test Matrix for 3 Level, 2 Factor full factorial design

Specimen number	Factor A	Factor B
1	0	0
2	1	0
3	2	0
4	0	1
5	1	1
6	2	1
7	0	2
8	1	2
9	2	2

3.4 Properties of Al-alloy for Additive Simulation

Although this study is meant to be for the AlSi10Mg alloy, due to lack of temperature specific properties in the literature, most of the properties derived are based on known room temperature range of AlSi10Mg with temperature dependent trend of Al-6061 alloy. Hence, the general terminology Al-alloy is used.

Aluminum alloys in general are arduous to be processed with laser due to their properties like high thermal conductivity, high coefficient of thermal expansion and mostly low energy absorptivity with highly reflective nature towards laser (Uddin, et al., 2016). In addition to this, they are also susceptible to hot tearing during solidification which is further exacerbated by rapid cooling rates and non-uniform solidification imposed by the laser melting process of AM (Fulcher, et al., 2014). However, addition of few percentage of silicon to aluminum is reported to significantly improve these properties (Fulcher, et al., 2014). The shrinkage due to coefficient of thermal expansion is substantially lowered and the solidification temperature range (i.e.$\Delta T = T_{liquid} - T_{solid}$) is also reduced from around 70K in Al6061 to 40K in AlSi10Mg which almost eliminantes the effect of hot cracking during solidification of the metal. Hence, due to relative ease of processing of AlSi10Mg alloys, they are preferred above other aluminum alloys such as Al6061 in laser processed metal 3D printing.

The part fabrication process in additive manufacturing involves transient thermal process coupled with both linear and non-linear static structural at each interval of temperature change. Hence, the properties ought to be defined should include the effects of temperature variation from room temperature to near melting point along with material specific non-linearity.

3.4.1 Density

It is a known fact that density defines the mass in a unit volume and mass directly links with specific heat of the material which is a crucial property that determines its temperature rise by some specific amount of applied heat. Since temperature specific density data for Al-6061 alloy is scarce in the literature, the trend of Al-7041 shown by Narender, et al., (2013), was followed from the point of known room temperature density of AlSi10Mg up to its melting point (660^0C).

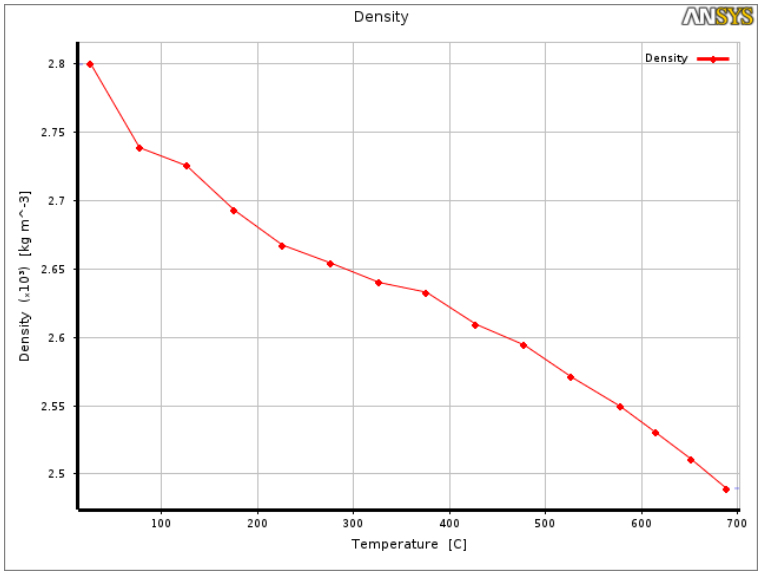

Figure 3-6 Density of Al-alloy as a function of temperature defined in ANSYS Workbench

3.4.2 Specific Heat

Specific heat of a material can be defined as the amount of heat required in order to raise the temperature of one gram of the material by one degree Celsius. Mathematically, $c = \frac{Q}{m \times \Delta T}$ where 'c' is specific heat capacity, 'Q' is heat energy added and 'ΔT' is the change in temperature. This property was estimated by Summers, et al., (2015) using laser flash diffusivity.

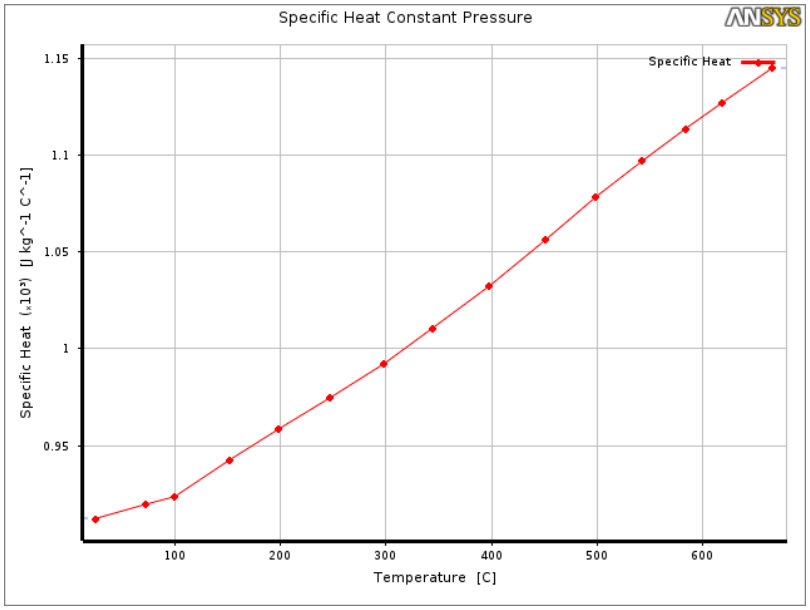

Figure 3-7 Temperature dependent specific heat capacity for Al-alloy defined in ANSYS Workbench

3.4.3 Thermal Conductivity

Thermal conductivity is the property of material that defines its ability to transfer/conduct heat from one point to another. Even though this is anisotropic property, it is assumed to be isotropic with respect to all directions. This is generally estimated by Fourier's law of heat conduction: $q = -k\nabla T$, where 'q' is the heat flux, 'k' is the thermal conductivity and $'\nabla T'$ is the temperature gradient. This property for Al-6061 has been estimated by Summers, et al., (2015).

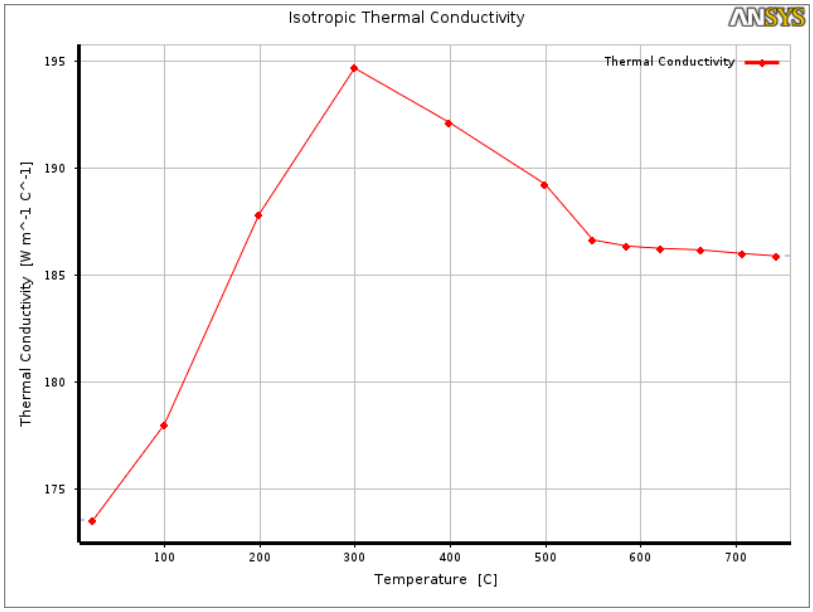

Figure 3-8 Temperature dependent thermal conductivity for Al-alloy defined in ANSYS Workbench

3.4.4 Coefficient of Thermal Expansion (CTE)

Coefficient of thermal expansion defines change in length, area and volume as a response to temperature variation. Mathematically, $\Delta L = \alpha L \Delta T$, where $'L'$ is the original length, ΔL is the change in length, ΔT is the temperature difference and α is the coefficient of thermal expansion. CTE for Al-6061 has been estimated by Summers, et al., (2015) and is assumed to be isotropic in the current study.

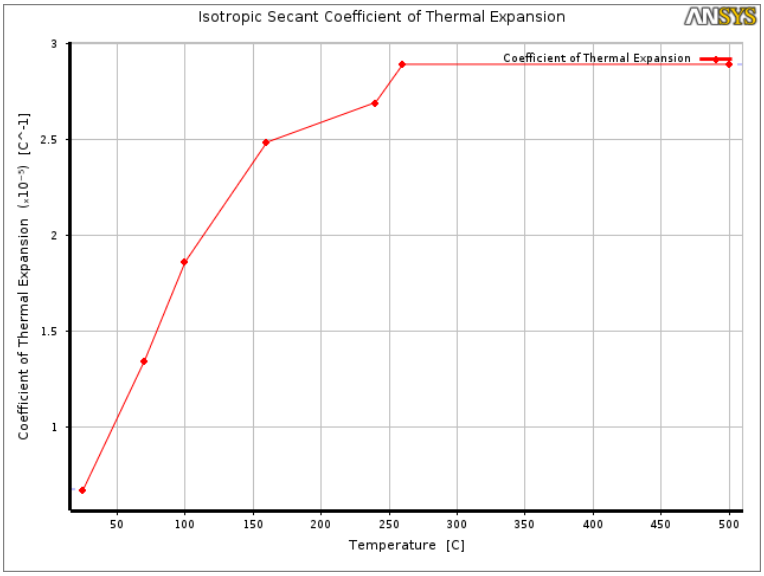

Figure 3-9 Temperature dependent CTE for Al-alloy defined in ANSYS Workbench

3.4.5 Young's Modulus and Poisson's Ratio

Young's Modulus or Modulus of Elasticity defines the linear region of the stress-strain curve of the material governed by the generalized Hooke's law. Mathematically, $E = \frac{\sigma}{\varepsilon}$, where E is the modulus of elasticity, σ is normal stress and ε is the normal strain. When metal 3D printing is considered, the laser melts the metal powder in horizontal direction and layers are stacked up vertically. This usually results in anisotropy in terms of strength of the material, however, for simplifying, such presence of anisotropy is ignored in the current study and is derived from work of Summers, et al., (2015).

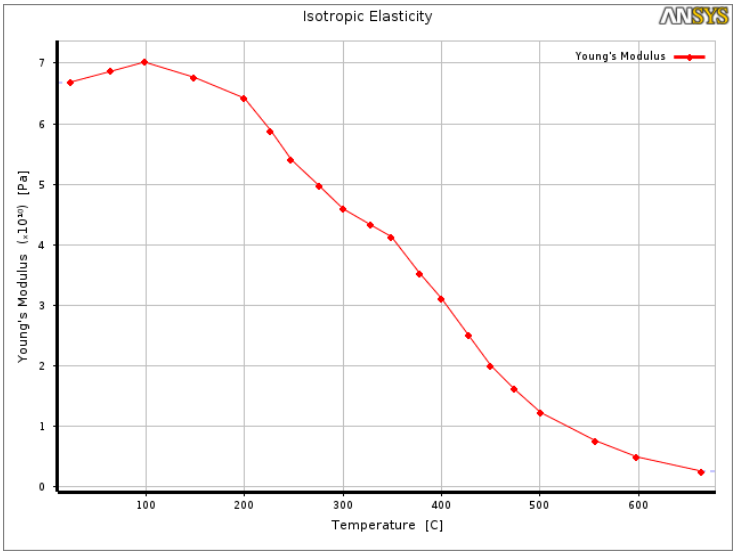

Figure 3-10 Temperature dependent Young's modulus for Al-alloy defined in ANSYS Workbench

3.4.6 Plastic Model (Bilinear Isotropic Hardening)

The plastic strains produced by stresses beyond yield is assumed to be defined by Bilinear Isotropic Hardening which is basically derived from the young's modulus, yield stress and tangent modulus of Al-6061 alloy obtained at different temperatures (Summers, et al., 2015).

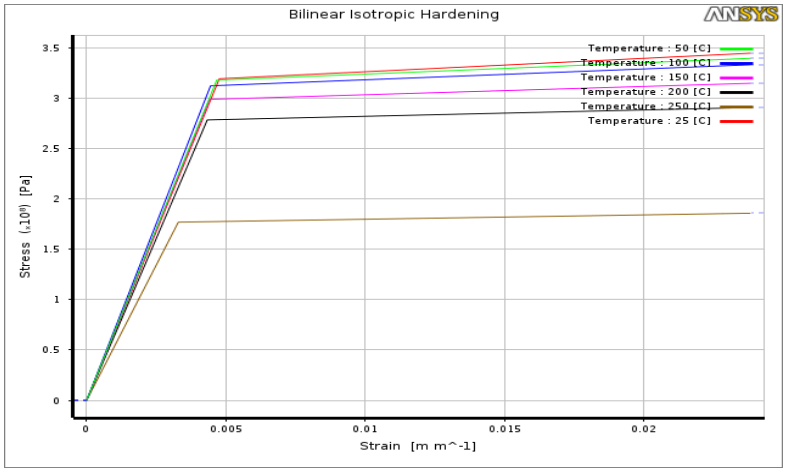

Figure 3-11 Temperature dependent stress-strain bilinear curve defined in ANSYS Workbench

The additive solver was actually developed by 3DSIM, LLC which was later acquired by ANSYS. The thermo-mechanical physics underneath the simulation process has been explained by Pal, et al., (2014) during 3DSIM software development phase. It accounts for three phases of the material i.e. powder, molten metal and solid along with temperature dependent thermo-physical properties. During the solution process, the powder properties are scaled based on packing density which can be defined with the powder property factor parameter. The solution works for a particular scan pattern of the laser which results in different thermal history with combination of finite element, eigen mathematics and periodicity. Since, the laser used would have same laser power and same scan speed throughout the build pertaining to a scan pattern, the solver takes heating side of the equation to be repeatable, however, for each scan vector, the cooling side is made different in order to facilitate the accumulation of varying thermal history of each layer throughout the build. The solver mathematically decomposes heating and cooling into different modes for solving the build process. As in a traditional finite element process, the

solver generalizes heat and strain accumulation then averages and stacks all the accumulated data.

3.5 SLM Process Parameters

The process parameters' values selected for the powder bed fusion process simulation are enlisted in the table below:

Table 3-2 Process parameters for additive simulation

Machine Setting	**Values**
Deposition thickness	$50\mu m$
Hatch Spacing	0.13 mm
Scan Speed	1200 m/s
Dwell Time	10 s
Number of heat sources	1
Build Conditions	
Preheat temperature	50^0C
Initial powder temperature	50^0C
Gas Convection Coefficient	1e-5 $\frac{W}{mm^2}.^0C$
Powder Convection Coefficient	1e-5 $\frac{W}{mm^2}.^0C$
Powder Property Factor	1e-2
Cooldown Conditions	
Room temperature	22^0C
Powder temperature	22^0C
Gas Convection Coefficient	1e-5 $\frac{W}{mm^2}.^0C$
Powder Convection Coefficient	1e-5 $\frac{W}{mm^2}.^0C$

3.6 Direct Interpolation for Stress Mapping

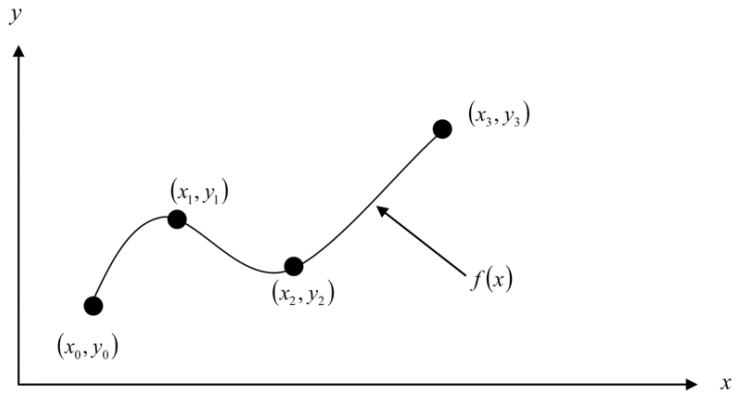

Figure 3-12 Interpolation function

Direct interpolation is basically related to fitting a polynomial equation from the sets of available discrete point after which data along the curve can be extracted. The process starts with assumption of polynomial equation with the order n as:

$$y = a_0 + a_1 x + a_2 x^2 \dots a_n x^n$$

We have (n+1) unknown coefficients i.e. ($a_o \dots a_n$). From the total number of discrete points available, we get (n+1) equations which can be used to estimate the coefficients.

In the current study, the averaged stress tensor is mapped as a function of nodal coordinate data of brick elements to corner nodes of the tetrahedral mesh. It is important to ascertain that both the meshes have same global coordinate system.

3.7 Multi-Objective Genetic Algorithm (MOGA) for Design Optimization

The design optimization problem in the current study consists of a multiple number of objectives that are to be achieved with definite sets of constraints applied. The objectives and constraints of the problem are outlined as follows:

- Minimizing mass of the structure
- Maximizing fatigue life for the given loading condition
- Keeping the distortion of the part to a minimum level by applying constraints

- Achieving a reasonable range of margin of safety with the help of constraints

Firstly, it should be noted that most of the optimization algorithms work for minimization, however, the objective function to be maximized can be converted to a minimization subroutine simply by considering negative value of the equation (Konak, et al., 2006). Konak, et al., (2006) have described the multi-objective design optimization in the following simple steps:

1) Initially, the design variable vector in the solution space is defined.
2) The problem is to find a vector that minimizes N number of objective functions.
3) The solution will be restrained and controlled by a set of constraints governing the system.

The above-mentioned steps are coupled with general genetic algorithm in order to complete the multi-objective genetic algorithm optimization. The procedure involved in this process is clearly explained in ANSYS-help, Multi-objective Genetic Algorithm (MOGA) section as follows:

Step-1: A set of initial population is defined.

Step-2: New set of population is generated with cross-over and mutation (using genetic algorithm) with a predefined value of number of samples to be created in a single iteration.

Step-3: The design points within the population is defined.

Step-4: The potential optimal solution obtained with the new set of population is checked for convergence which returns a true value when maximum allowable Pareto Percentage is reached and stops the optimization else the algorithm proceeds to step-5.

Step-5: The maximum number of iterations ran is validated as a stopping criterion of the process. If this returns a true signal, the optimization process is stopped else it proceeds to step-2. The procedure repeats until either the stopping criterion is reached, or the solution is converged.

The process to generate the new set of population using genetic algorithm (GA) in Step-2 of above optimization algorithm is described in the ANSYS-help, Multi-objective Genetic Algorithm (MOGA) section as following:

3.7.1 Cross-over

This creates a new data point (offspring) using two parent data points (or chromosomes) with an assumption that the offspring inherit good characteristics from the parent data points and better aid the optimization process. For continuous design points, the parent data points are combined with a linear equation whereas, for discrete points, the cross-over takes place in binary form (each digit known as a gene) of the data points as illustrated in figure 3-12.

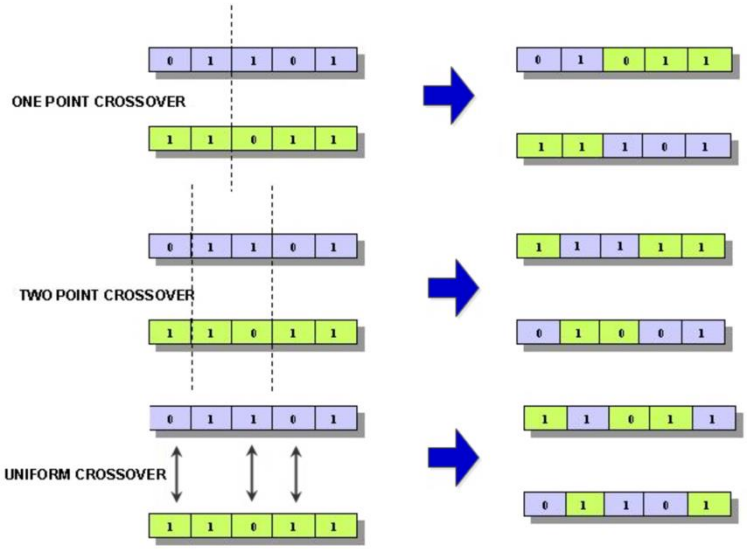

Figure 3-13 Different types of discrete crossover

(source: https://www.sharcnet.ca/Software/Ansys/17.0/en-us/help/wb_dx/dxBEMtemp11.html)

3.7.2 Mutation

This process causes alteration in genes within a chromosome resulting in an entirely new design point which may bring the optimization process at a relatively better boundary to where it was before. This is a crucial part of GA that aids the data points from being dormant to a local solution, however, mutation process is a complete probabilistic approach. Furthermore, for continuous parameters, mutation occurs with a polynomial mutation operator fitted in the linear equation, whereas, 0 and 1 are inverted with a probability of 0.5 for discrete parameters.

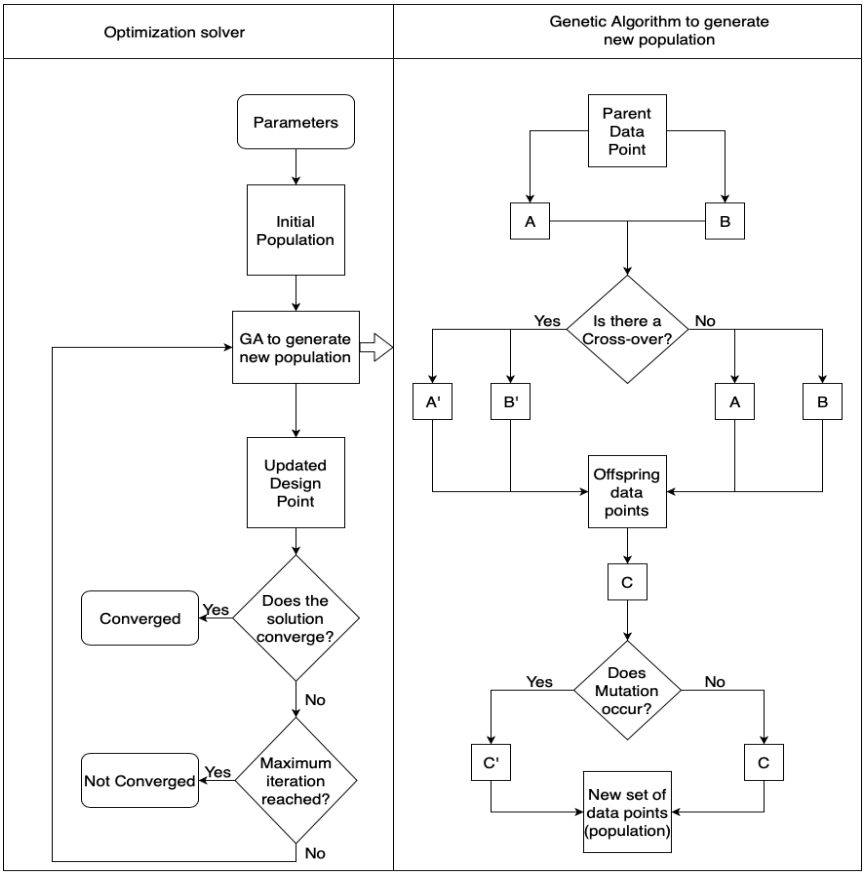

Figure 3-14 Flowchart for MOGA (derived from:

https://www.sharcnet.ca/Software/Ansys/17.0/en-us/help/wb_dx/dxBEMtemp11.html

3.8 Finite Element Model Setup for AM Simulation

Generally, a finite element analysis comprises of three steps: pre-processing (defining a problem), processing (solving governing equations) and post-processing (visualization of the result). The user inputs during pre-processing of the finite element analysis are defined and illustrated as follows:

3.8.1 CAD Model of the Part and Support Structure

Part:

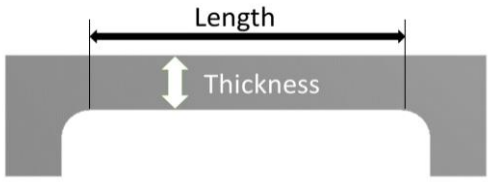

Figure 3-15 CAD model of the bridge

Total of 9 bridge shaped specimens are defined for 3^2 full factorial DOE study. The combination of length and thickness for each specimen is shown in the table below:

Table 3-3 Part Dimensions

Specimen	Length (mm)	Thickness (mm)
1	35	5
2	50	5
3	65	5
4	35	7.5
5	50	7.5
6	65	7.5
7	35	10
8	50	10
9	65	10

Supports:

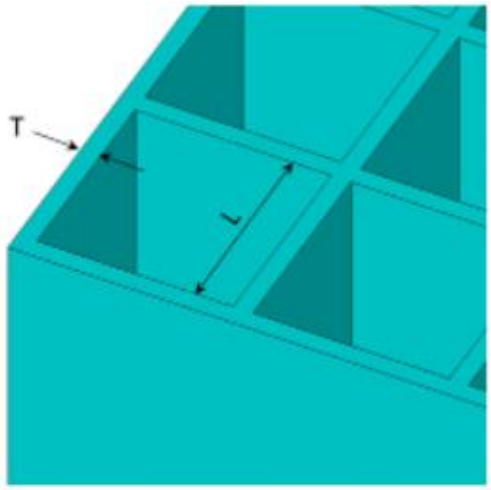

Figure 3-16 Block type supports

The properties of the support structure are homogenized with a desirable configuration of the support lattice defined within ANSYS Workbench's Additive Suite. This saves computation power by not including complex geometry of the lattice which cannot be captured without an ultra-fine mesh.

The wall-spacing and thickness used for the support group are:

Wall spacing (L): 1.9366 mm

Wall thickness (T): 1.0634 mm

The supports used have the properties adjusted according to above dimensions. The affected properties are elastic modulus, shear modulus, stiffness, density and thermal conductivity.

3.8.2 Mesh

Additive simulation requires elements with uniform thickness throughout the build. Hence, the mesh type selected for the entire additive process is of the cartesian form i.e. with linear brick elements. This causes stair step effect in the curvature of the geometry.

Also, the size of each element is limited by powder particle size. It has been suggested in ANSYS guidelines to use the element size of least 5 to 10 times the deposition thickness. Consequently, 0.5 mm element size was used for the deposition thickness of 50 μm.

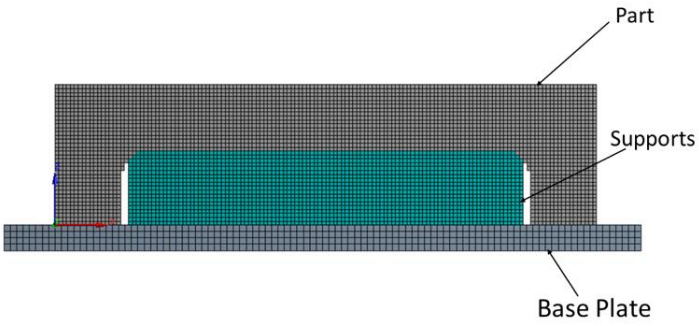

Figure 3-17 Mesh for additive simulation

The stress data from cartesian mesh is to be transferred to higher order mesh using interpolation where the superposition effect is simulated. The quadratic tetrahedral mesh with element size 0.5 mm is shown in figure 3-18.

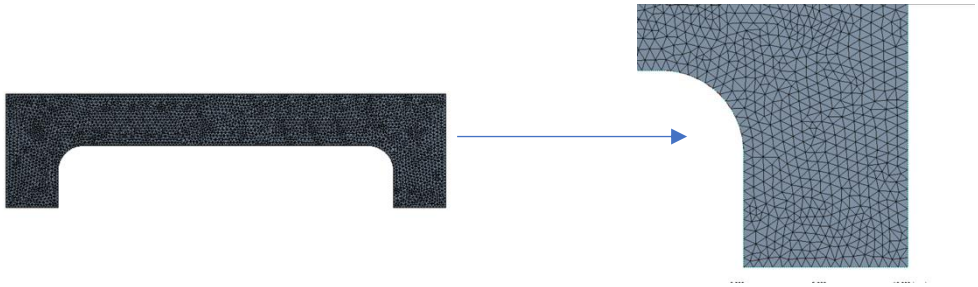

Figure 3-18 Mesh for static structural simulation

3.8.3 Boundary Conditions

Additive simulation:

For thermal analysis, the bottom face of the base plate was supplied a pre-heat temperature of 50^0C. The build boundary temperature was also specified as 50^0C and the cooldown temperature as 22^0C.

For structural analysis, again the bottom face was selected as a fixed support which is valid before removal of the part from the base plate. To simulate the relaxation post removal of the base plate and support, the left bottom face of the part was fixed in space. The load applied is the variation of temperature in each layer during time dependent thermal analysis of the build.

Service stress simulation:

The residual stress tensor data from AM simulation was transferred to an undeformed model after which modified sequential boundary and loading conditions were applied as following:

1) Two remote points (right bottom face and a line at the top surface where point load acts) were defined and assigned a variable using following snippets:
   a) right_pilot=_npilot
   b) top_pilot=_npilot

   The "_npilot" is the collection of nodes of interest. After the remote points are designated, the left bottom surface is kept fixed throughout all the loading steps.
2) In the first loading step, residual stresses are applied as imported initial loads to produce deformations.
3) In the second step, a boundary condition is applied to fixate "right_pilot" node in all degrees of freedom using the following snippet:

   d,right_pilot,ALL,%_FIX%
4) In the final step, a line force of 3000 N is applied at the "top_pilot" node using:

   F,top_pilot,FZ,3000

Chapter 4

Results and Discussion

First, the temperature distribution throughout the build process was simulated in a transient environment where each layer was assigned with heat applied and cooldown step. This temperature data from each step was transferred to AM structural simulation for the prediction of residual stresses. Subsequently, the residual stress tensor data before removal of supports and base plate was applied to an undeformed model in another structural analysis so that the model could be prestressed before any external load is applied with new boundary conditions. Figure 4-1 summarizes all these steps.

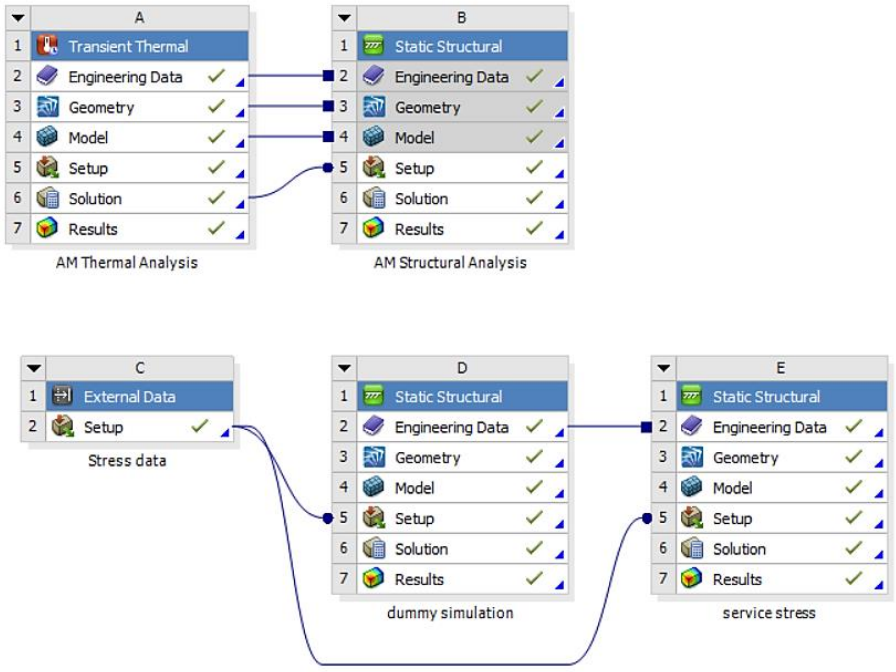

Figure 4-1 Steps involved in estimating the service stress (in ANSYS Workbench)

4.1 Temperature Profile

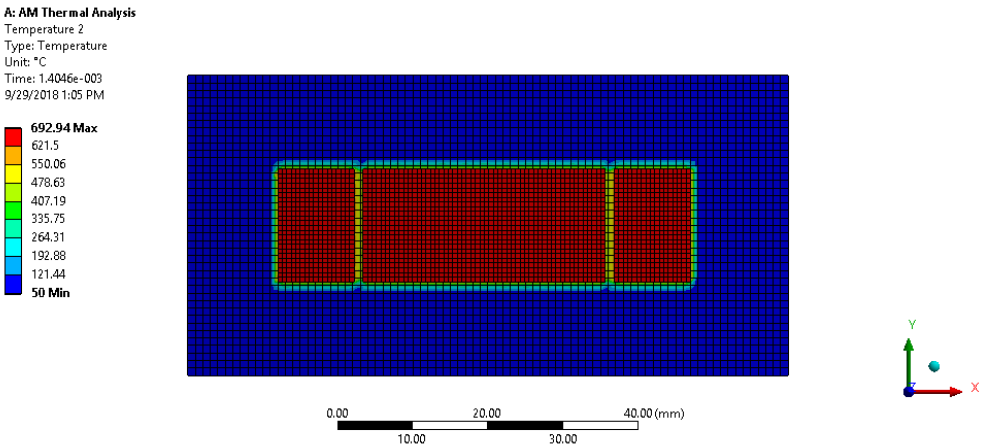

Figure 4-2 Temperature Profile after melting of first layer (specimen 1)

The temperature profile of all the specimens are similar as they are subjected to the same boundary temperatures with same melting point during each layer build. Figure 4-2 shows the temperature profile in the first added layer after the powder particles are melted. The base plate acts as a heat sink and thus, heat is dissipated through the base plate as illustrated in figure 4-3.

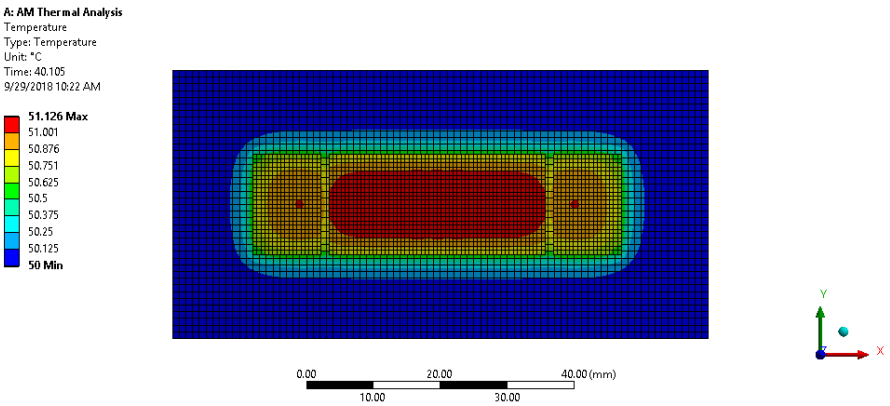

Figure 4-3 Dissipation of heat in the first layer to the base plate (specimen 1)

After the final layer is deposited and melted, the build cools down to room temperature of 22^0C. The dissipation of heat after the final layer is melted is shown in figure 4-4.

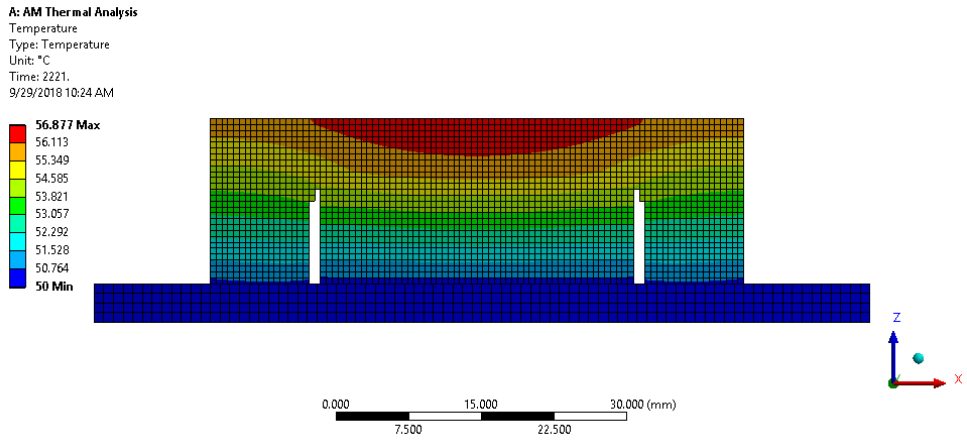

Figure 4-4 Heat dissipation as the part cools down after final layer is melted (specimen-1)

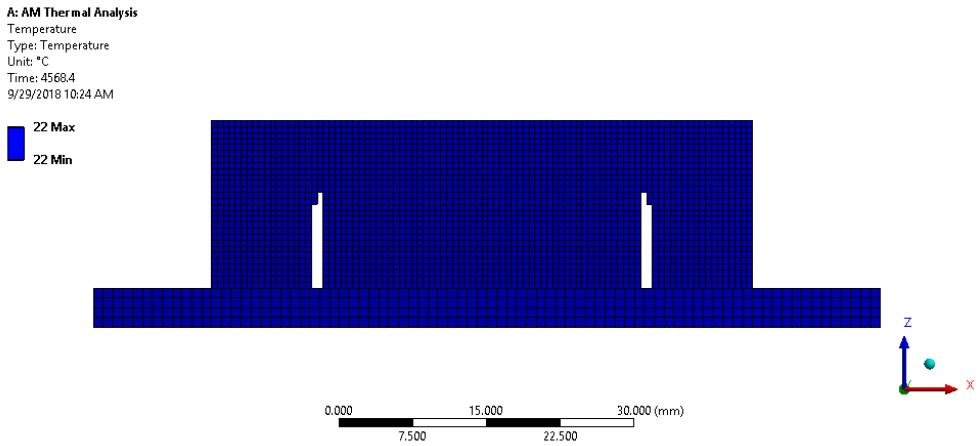

Figure 4-5 Room temperature cooldown (specimen-1)

All these differential temperatures act as loads in the coupled structural analysis which causes stress build up in the part.

4.2 Thermo-Structural Analysis Results

4.2.1 Stresses in x-direction from additive simulation:

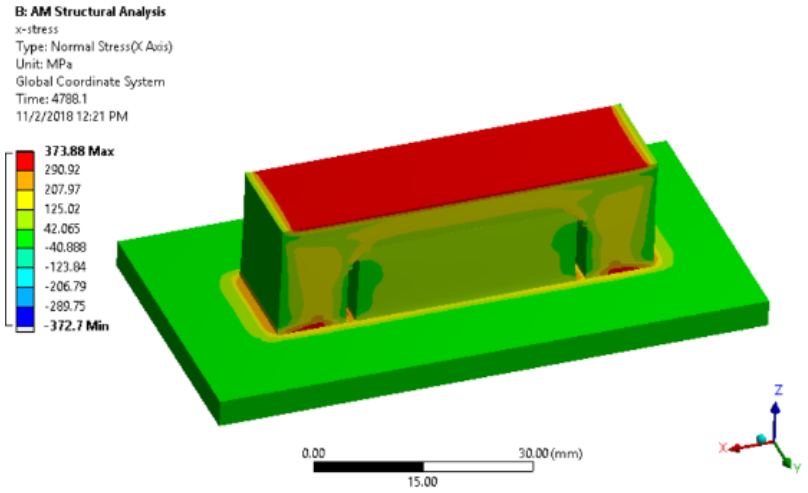

Figure 4-6 X-directional stresses post build (Specimen 1)

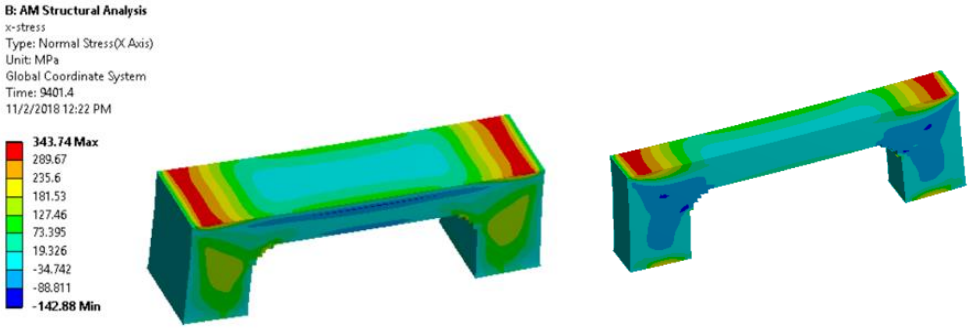

Figure 4-7 Stresses in x-direction after relaxation with sectional view (Specimen-1)

During the build process, the x-directional stresses (σ_x) develop along the direction of laser scan due to expansion restriction in heating and contraction restriction in cooling process along x-direction by the surrounding material. As it can be seen in figure 4-7, the tensile stresses act on the surface of the part with a peak value of +374 MPa while the compressive stresses are present in the core with peak value of -373 MPa. Some amount of these significantly high value of stresses tend to relaxation after the removal of base

plate and support structure which is shown in figure 4-7. Consequently, the maximum tensile stress reduces from +374 to +344 MPa whereas, the peak value of compressive stress shows a larger difference i.e. it reduces from -373 MPa to -143 MPa.

The results for peak stresses in x-direction for all the specimens are tabulated as:

Table 4-1 Stresses in x-direction

Specimen	Tensile post-Build (MPa)	Tensile post-removal (MPa)	Compressive Post-build (MPa)	Compressive Post-removal (MPa)
1	+373.88	+343.74	-372.7	-142.88
2	+378.1	+345.5	-328.82	-142.41
3	+380.39	+346	-305.18	-143.28
4	+369.09	+346.17	-349.81	-142.9
5	+373.83	+347.79	-283.73	-142.12
6	+377.63	+348.67	-165.47	-142.38
7	+366.75	+348.9	-289.1	-136.88
8	+372.08	+350.39	-204.26	-136.63
9	+376.33	+351.53	-183.09	-136.56

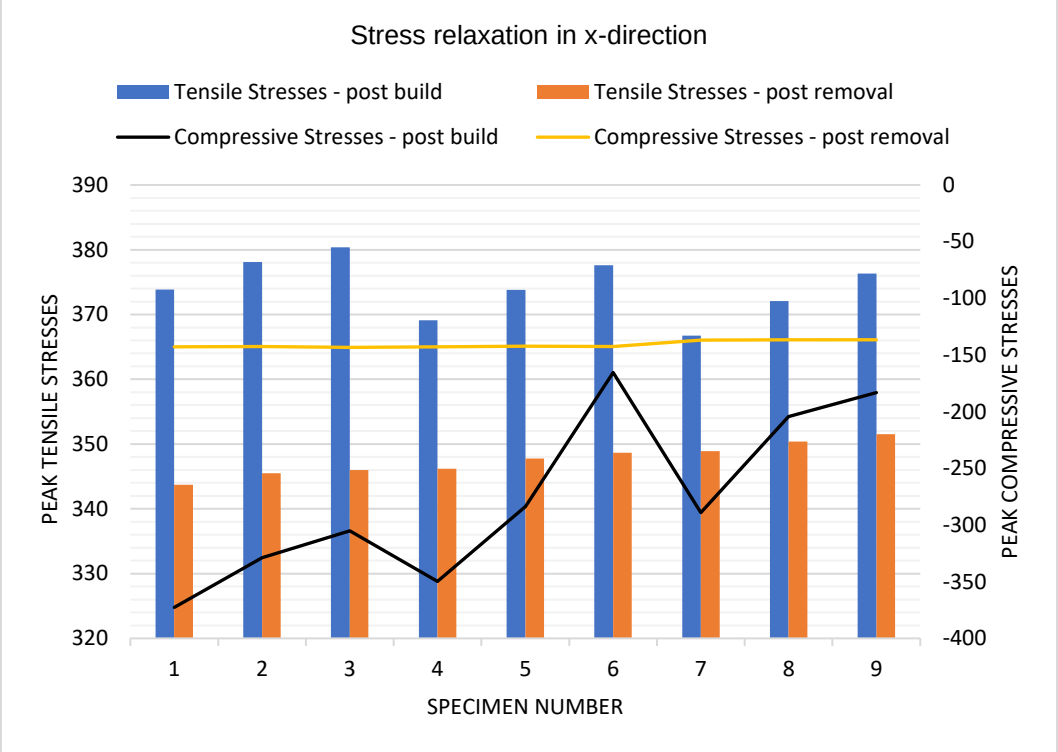

Figure 4-8 Stresses in x-direction pre and post removal of base plate and supports

Figure 4-8 shows stress state in x-direction when the build is complete and when it has been removed from base plate and support for all the 9 specimens. The peak tensile and compressive stresses post relaxation is almost equal in all specimens which can be attributed to plastic strains produced in the peak stressed regions.

4.2.2 Stresses in z-direction from additive simulation:

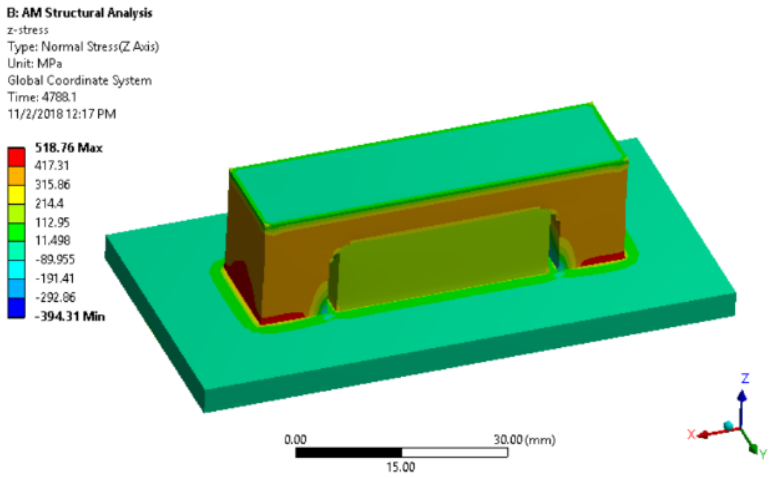

Figure 4-9 Z-directional Stresses post build (specimen-1)

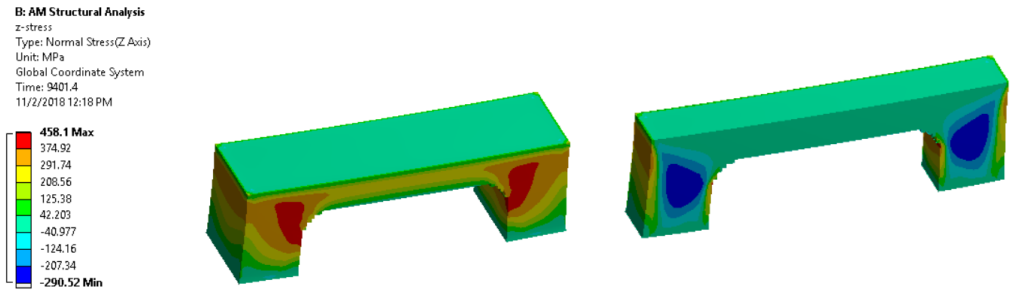

Figure 4-10 Stresses in z-direction after relaxation with sectional view (specimen-1)

Z-direction is the build direction along which the layers are stacked upon. It can be seen in figure 4-9, since the part has been anchored in the base plate, the deformation in the vertical direction is restricted and hence the stresses develop. Figure 4-10 shows the relaxed stress state after removal of the support and base plate. Post relaxation, the peak tensile stress in the surface reduce from +518 MPa to +458 MPa, whereas, compressive stresses reduce from -394 MPa to -290 MPa. The peak stresses in z-direction for all the specimens are shown in table 4-2.

Table 4-2 Stresses in z-direction

Specimen	Tensile post-Build (MPa)	Tensile post-removal (MPa)	Compressive Post-build (MPa)	Compressive Post-removal (MPa)
1	+518.76	+458.1	-394.31	-290.52
2	+523.04	+457.63	-382.27	-289.98
3	+525.48	+459.57	-383.93	-289.67
4	+523.38	+458.99	-394.82	-317.94
5	+528.91	+459.45	-391.75	-317.85
6	+532.16	+437.27	-374.22	-313.74
7	+523.68	+457.98	-396.47	-331.85
8	+530.49	+458.622	-380.19	-333.08
9	+534.9	+459.21	-368.76	-333.43

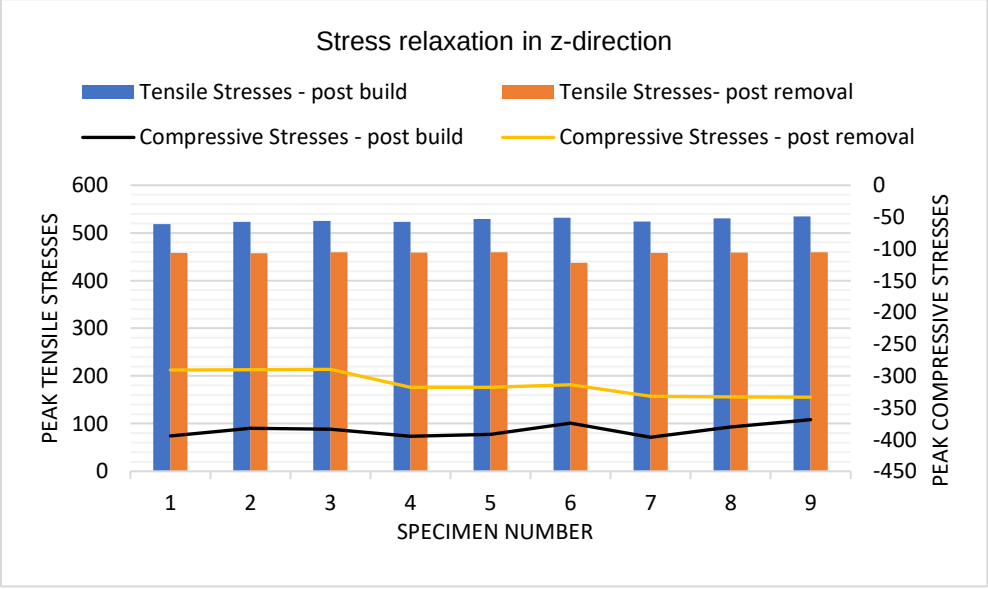

Figure 4-11 Stresses in z-direction pre and post removal of the base plate and supports

4.2.3 Von Mises Stress from additive simulation

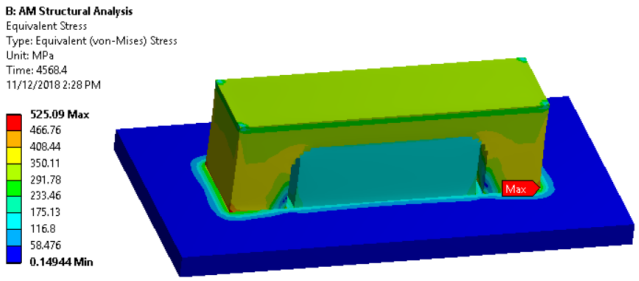

Figure 4-12 Von Mises Stress post build (specimen-1)

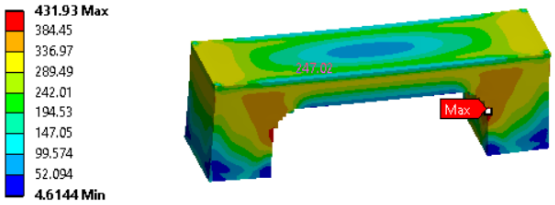

Figure 4-13 Von Mises stress after relaxation (specimen-1)

The maximum Von Mises Stress is concentrated at the corners of the part after the build is complete which is shown in figure 4-12 as it was shown by Vrancken (2016). It can be predicted that these corners might crack out during the removal process from the base plate. The stress concentration, however shifts to the fillet of the overhang illustrated in figure 4-12 after the removal of baseplate and supports.

4.2.4 Distortion Results

The Z-deformation results after removal of the base plate and the supports are shown in figure 4-14.

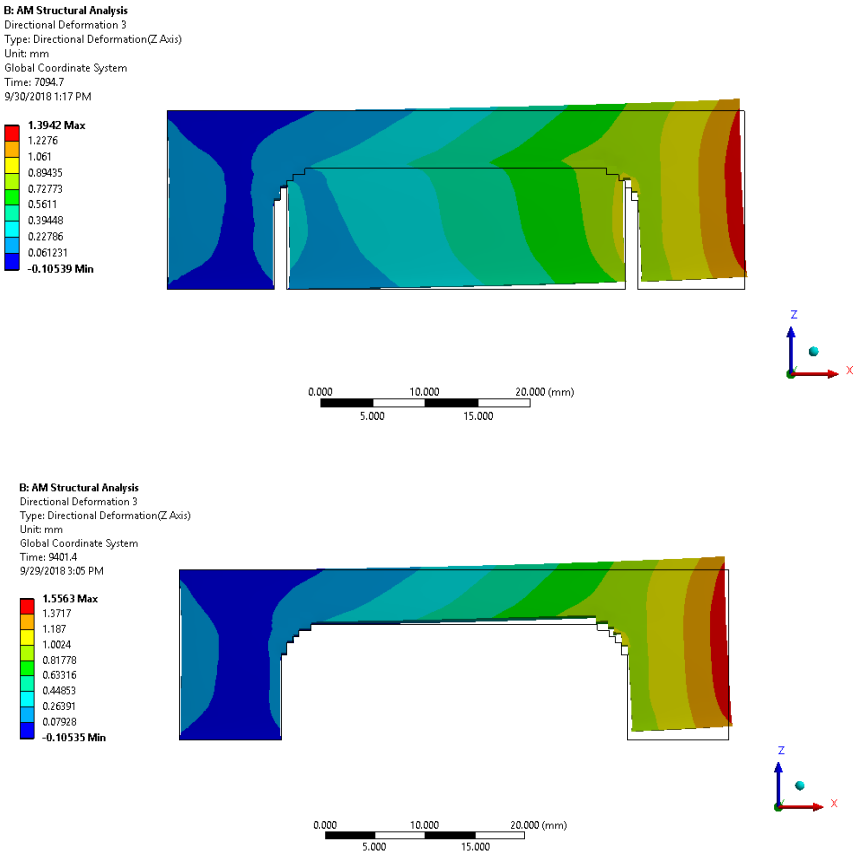

Figure 4-14 Z-directional deformation before removing supports (top) and after removing supports (bottom) (specimen -1)

The distortion is caused by stress relaxation primarily in the form of shrinkage and warping. Warping is more prominent which is caused by the stresses in x and z directions. It can be visualized in figure 4-14 that as the base plate is removed, specimen-1 starts distorting to about 1.39 mm and this deformation further increases to 1.55 mm after removal of the supports. The deformation pattern in the entire set of specimens is similar, however, the magnitudes vary according to the length and thickness of the parts.

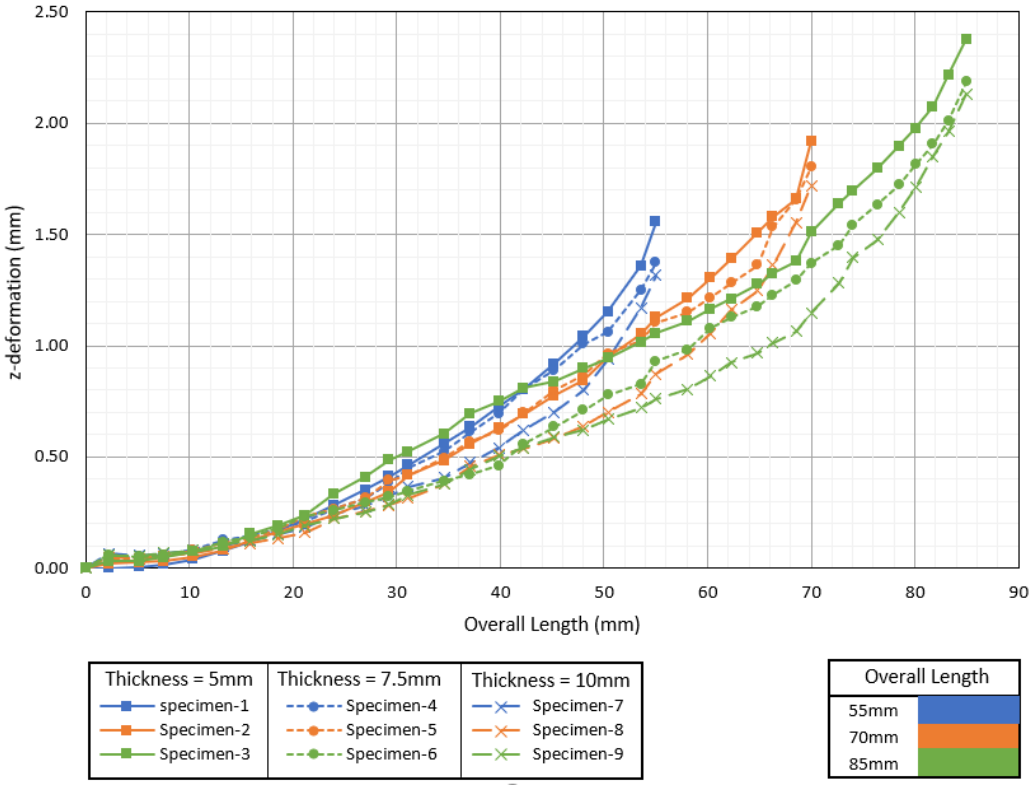

Figure 4-15 Deformation in z-direction Vs overall length of the specimens

It can be inferred from figure 4-15 that for specimens with same length, lesser the thickness more will be the z-deformation and vice versa. While for the specimens with same thickness, higher length values tend to show more deformation.

4.3 Service Stress (and Strain) Simulation

Here, the residual stresses are superimposed with the stresses due to applied external load (applied at the middle of the overhang). It was observed that the residual stresses applied in the initial step (as imported load) caused plastic deformation in all the specimens at some vulnerable regions (hotspots) which was amplified by the external force (applied in the final step of the analysis).

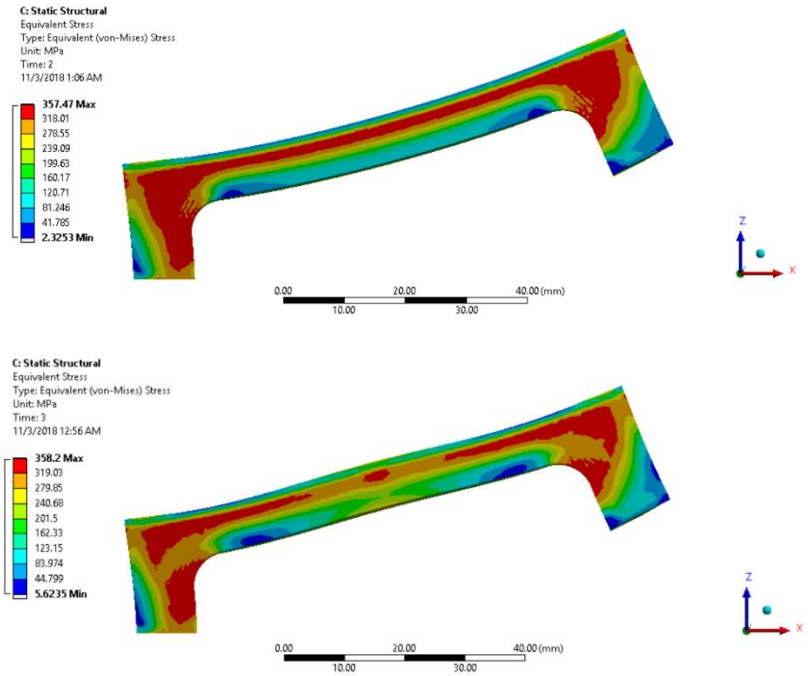

Figure 4-16 Von Mises stress state in specimen-3 before (top) and after (bottom) application of the external load [deformations shown are scaled by 5x]

It is illustrated in figure 4-16 that the peak Von Mises (357 MPa) residual stresses in specimen-3 is higher than the yield stress (i.e. 319 MPa) of the material due to which plastic strains are induced in some regions. The superposition further causes the peak stress to increase to 358 MPa while the average stress in the model is increased from 137 MPa to 146 MPa. The plastic strains in vulnerable regions are shown in figure 4-17.

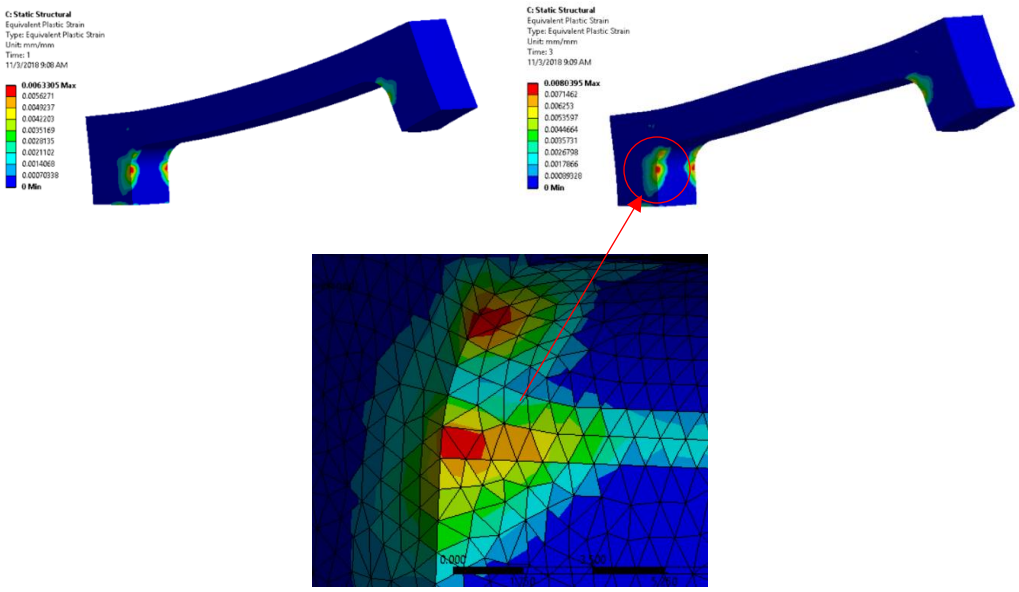

Figure 4-17 Equivalent plastic strains before (left) and after (right) superposition in specimen-3

A continuous unaveraged stress/strain field among adjacent elements signifies a converged solution in terms of stresses and strains. From the zoomed image of unaveraged plastic strains in figure 4-17, it can be said that there is some level of discontinuity present in the result along the tetrahedral elements which infers that the strains have not converged. Hence, all further calculations based on the strain amplitudes should only be taken as a process of establishing parametric equation and not be relied upon actual data.

4.4 Fatigue Life Calculation

The plastic strains before and after superposition for all the specimens are shown in the table below:

Table 4-3 Plastic Strain Amplitudes

Specimen	ε_{p_1}(mm/mm)	ε_{p_2}(mm/mm)	$\frac{\Delta\varepsilon_p}{2}$
1	5.86E-03	7.08E-03	6.11E-04
2	5.78E-03	7.38E-03	7.98E-04
3	6.52E-03	8.39E-03	9.37E-04
4	6.06E-03	7.29E-03	6.13E-04
5	6.81E-03	8.19E-03	6.91E-04
6	6.29E-03	7.79E-03	7.51E-04
7	5.10E-03	6.12E-03	5.08E-04
8	5.21E-03	6.33E-03	5.57E-04
9	5.24E-03	6.56E-03	6.60E-04

With plastic strains occurring at vulnerable regions, the failure mode is assumed to be with plastic deformation in the low cycle regime.

Using equation 2.2.3 i.e. Coffin Manson's equation from chapter 2,

$$\frac{\Delta\varepsilon_p}{2} = \varepsilon_f'(2N)^c$$

With $\varepsilon_f' = 0.11$ and $c = -0.6$, the total number of cycles evaluated for each specimen is shown in figure 4-18.

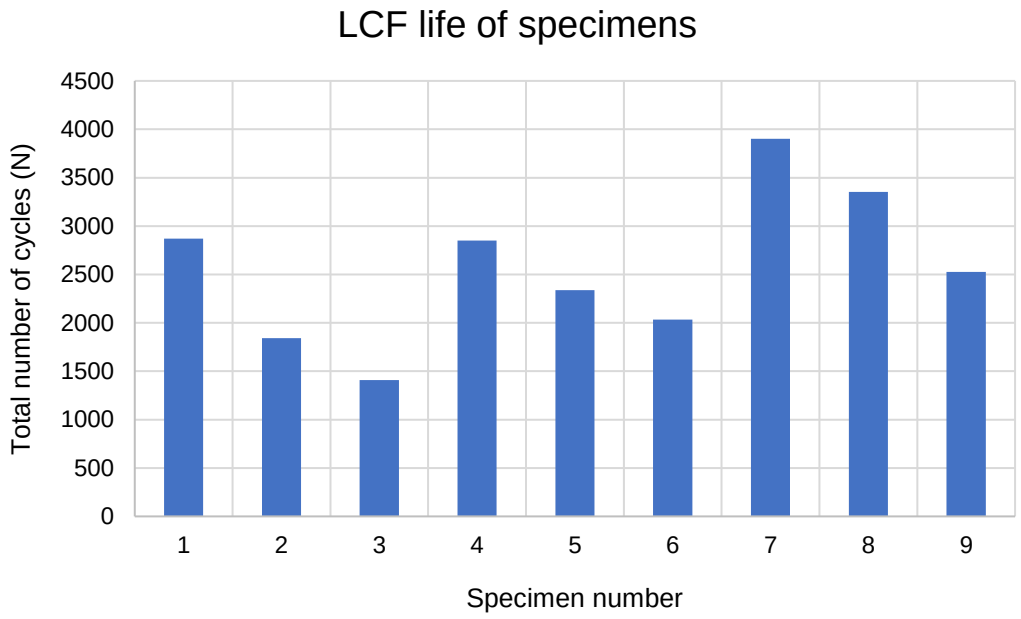

Figure 4-18 LCF life of specimens

It can be seen from figure 4-18 that Specimen-7 (shortest and thickest) can bear highest number of cyclic loads with about 3900 cycles while Specimen-3 (longest and thinnest) has relatively shortest life with only 1408 cycles.

4.5 Response Surface Models

The assumption for LCF life in terms of length and thickness of the specimens is a full quadratic equation:

$$N_f = a_0 + La_1 + Ta_2 + a_3L^2 + a_4T^2 + a_5LT + \epsilon$$

Since we have 9 equations and 6 unknowns, we can calculate the coefficients using equation 2.5.6 mentioned in chapter 2. This equation takes the form,

$$\begin{Bmatrix} a_0 \\ a_1 \\ \vdots \\ a_5 \end{Bmatrix} = \left(\begin{bmatrix} 1 & L_1 & T_1 & L_1^2 & T_1^2 & L_1T_1 \\ 1 & L_2 & T_2 & L_2^2 & T_2^2 & L_2T_2 \\ \vdots & \vdots & \vdots & \vdots & \vdots & \vdots \\ 1 & L_6 & T_6 & L_6^2 & T_6^2 & L_6T_6 \end{bmatrix}' \begin{bmatrix} 1 & L_1 & T_1 & L_1^2 & T_1^2 & L_1T_1 \\ 1 & L_2 & T_2 & L_2^2 & T_2^2 & L_2T_2 \\ \vdots & \vdots & \vdots & \vdots & \vdots & \vdots \\ 1 & L_6 & T_6 & L_6^2 & T_6^2 & L_6T_6 \end{bmatrix} \right)^{-1}$$

$$\begin{bmatrix} 1 & L_1 & T_1 & L_1^2 & T_1^2 & L_1T_1 \\ 1 & L_2 & T_2 & L_2^2 & T_2^2 & L_2T_2 \\ \vdots & \vdots & \vdots & \vdots & \vdots & \vdots \\ 1 & L_6 & T_6 & L_6^2 & T_6^2 & L_6T_6 \end{bmatrix} \begin{Bmatrix} N_{f1} \\ N_{f1} \\ \vdots \\ N_{f6} \end{Bmatrix}$$

So, the response surface equation for LCF life is,

$$N_f = 5859.3 - 98.5426L - 229.8T + 0.5170L^2 + 29.6533T^2 + 0.58LT$$

The response surface can be visualized in the figure below:

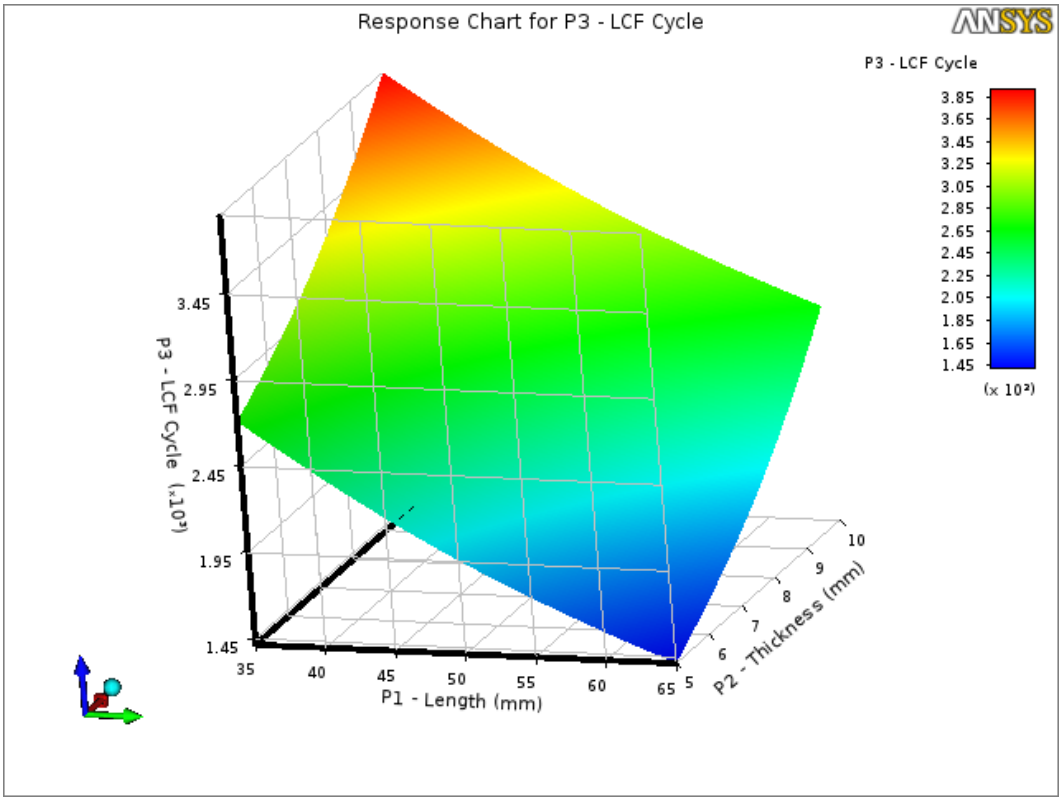

Figure 4-19 Quadratic response surface for LCF life

Similarly, the assumed equation for Z-deformation in terms of length and thickness of the specimens:

$$Z = a_0 + La_1 + Ta_2 + a_3L^2 + a_4T^2 + LTa_5a_6 + \epsilon$$

Again, calculating the coefficients using equation 2.5.6 shown in chapter 2, the response surface equation for the Z-deformation is,

$$Z = 1.2565 + 0.0242L - 0.1587T + (3.7E - 05)L^2 + 0.0077T^2 - (6.67E - 05)LT$$

Figure 4-20 shows the generated response of the deflection.

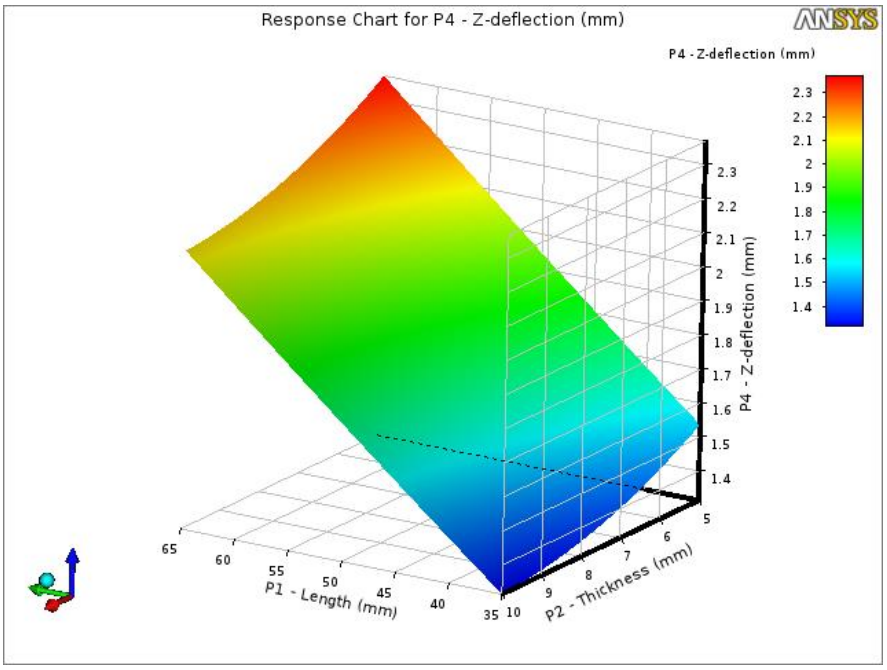

Figure 4-20 Quadratic response surface for Z-deflection

Increasing fatigue life and decreasing the z-deformation with mass is certain to over-design the model in terms of its static strength. In order to control this, the equation of factor of safety (FOS) was developed for same magnitude of load in absence of the residual strains and constrained to a reasonable range (1.5 to 2.7) for the optimization process.

Similar to the case of fatigue life and Z-deformation, the quadratic equation for factor of safety developed is:

$$FOS = 0.6519 - 0.0683L + 0.6907T + (7.2593E - 04)L^2 - 0.0011T^2 - 0.0055LT$$

The response surface for FOS is shown in figure 4-21.

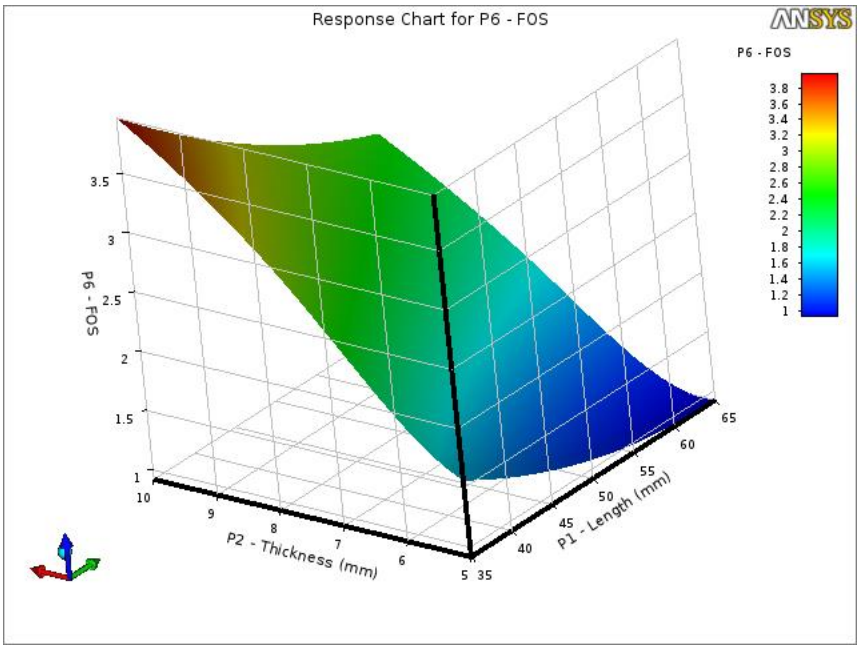

Figure 4-21 Quadratic response surface for Factor of Safety

The coefficients of response surfaces are given is table

Table 4-4 Coefficients of the regression models

Responses	a_0	a_1	a_2	a_3	a_4	a_5
LCF life	5859.3	98.5426	229.8	0.5170	29.6533	0.58
Z distortion	1.2565	0.0242	0.1587	$3.7E-05$	0.0077	$6.67E-05$
FOS	0.6519	0.0683	0.6907	$7.26E-4$	0.0011	0.0055

Quality of fit:

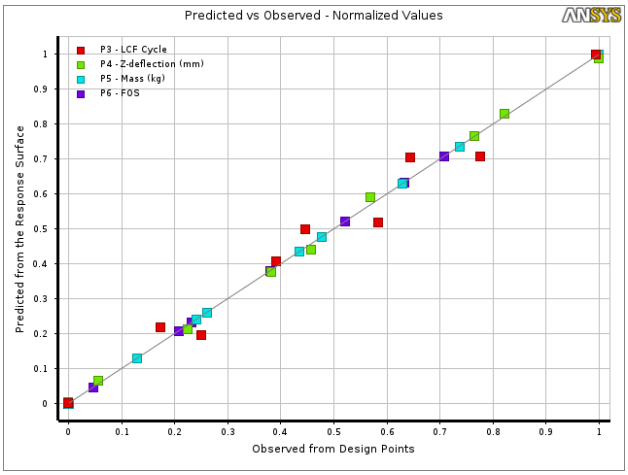

Figure 4-22 Goodness of fit of the response surfaces

The quality of fit of the generated response is shown in figure 4-22. The coefficient of determination which gives a measure of difference between actual response and that predicted by the regression model equation can be shown mathematically as,

$$\text{COD}=1-\frac{\sum_{i=1}^{N}(y_i-\hat{y}_i)^2}{\sum_{i=1}^{N}(y_i-\bar{y})^2}$$

y_i is the actual value of output parameter, $\hat{y}_i$ is the response predicted by the regression equation and $\bar{y}$ is the arithmetic mean value of y_i. If COD=1, it means that all the variation is perfectly predicted by the response model. The COD evaluated for the response surface equations generated in the current study are listed below:

Low cycle fatigue response: 0.97337

Z-deflection response: 0.99864

Factor of Safety response: 1

Main effects

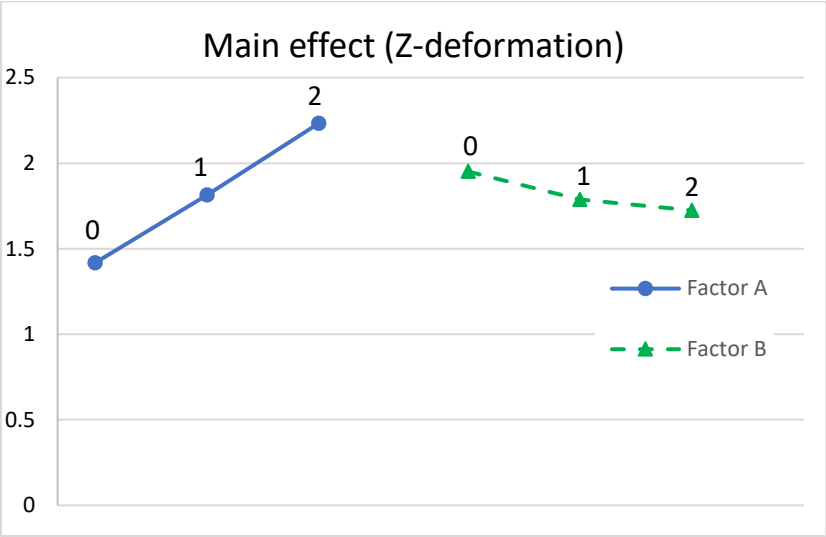

Figure 4-23 Factor experiment - main effect in z-deformation

The main effects of the 3^2 factorial experiment is summarized in figure 4-23 and 4-24. This explains the averaged effect of variation of factor A (length) over 3 levels while the factor B (thickness) is held constant and the averaged effect of variation of factor B over 3 levels while factor A is held constant. It can be inferred from figure 4-23 that variation of length over 3 levels has relatively more pronounced effect on the deformation result from additive simulation.

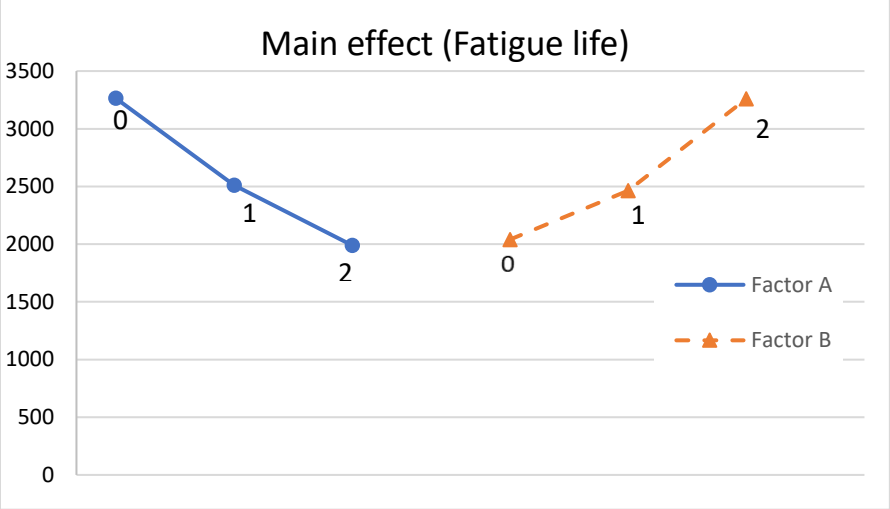

Figure 4-24 Factor experiment - main effect in fatigue life

Figure 4-24 infers that both the factors (A and B) are substantially sensitive to fatigue life. An increase in length for constant thickness degrades the total number of cycles before failure while increasing thickness for constant length has an opposite effect on the fatigue life.

Interactions

Interactions signify whether the performance of factor A in 3 levels is affected by the performance of 3 levels of factor B. Figure 4-25 and 4-26 summarizes this effect. It can be inferred from figure 4-25 that the difference in Z-deformation from additive simulation across different factor A levels is not very significant across the levels of factor B.

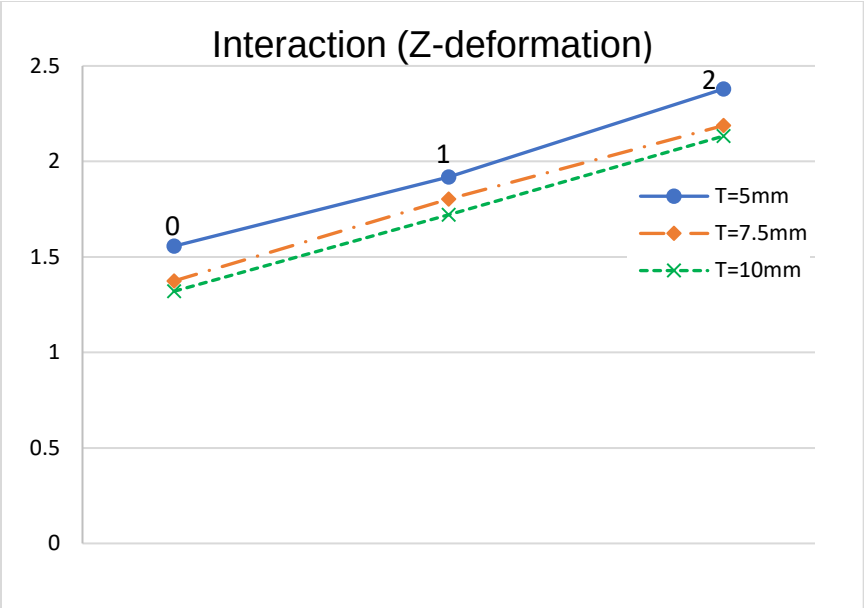

Figure 4-25 Factor experiment - interaction in z-deformation

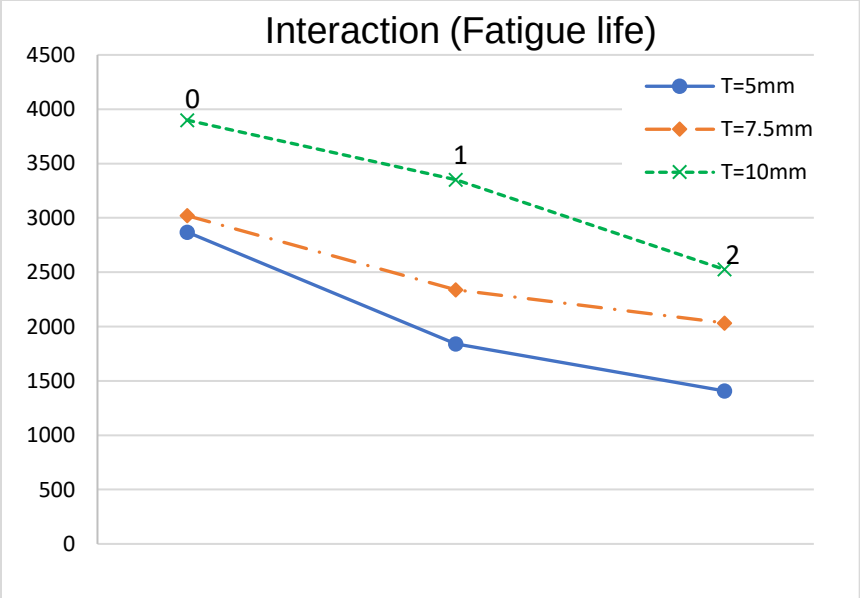

Figure 4-26 Factor experiment - interaction in fatigue response

Small variation is observed in fatigue life response at different levels of length of the overhang across different thickness levels as shown in figure 4-26. It can be said that

there is a presence of small interaction among these factors in determining the fatigue life of the parts.

4.6 Design Optimization

4.6.1 Optimization run using MOGA

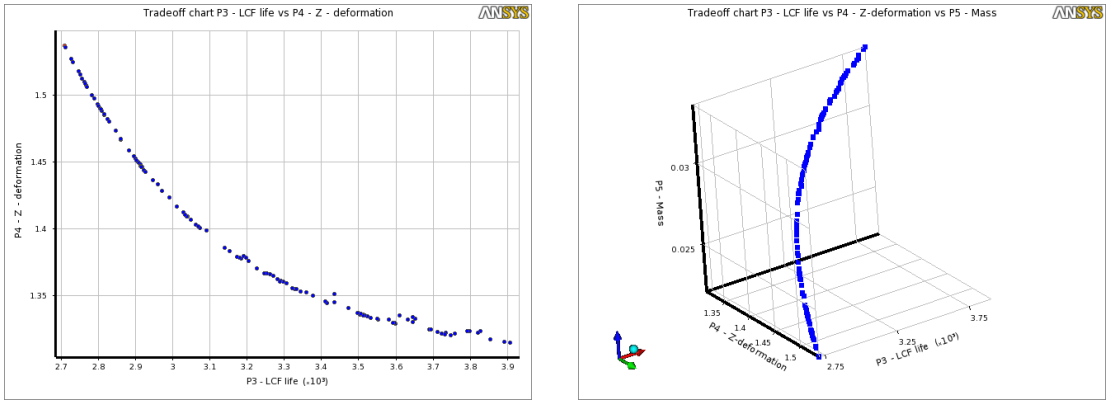

Figure 4-27 First Pareto front in 2D (left) and 3D (right)

Figure 4-27 shows the tradeoffs among various responses of the system when unconstrained multiple objectives are defined. The blue points designate feasible solution space where the objectives can be best achieved. It can be clearly seen that parts with higher fatigue life possess less distortion which is a desirable relation. Hence, in order to obtain a desirable specific solution, the objectives and constraints were defined as:

1) Maximize LCF life
2) Minimize mass
3) Minimize Z-deflection (with constraint: $1.3\ mm \leq Z \leq 1.4\ mm$)
4) Seek target of FOS as 1.5 (with constraint: $1.5 \leq FOS \leq 2.7$)

The optimization code for Multi-Objective Genetic Algorithm was run in ANSYS, however, the equations and results were also cross verified using the same optimization code in MATLAB (given in appendix). With this, the optimum point was obtained after 669 evaluations with the following dimensions,

Length (L) = 35.216 mm

Thickness (T) = 7.188 mm

Figure 4-28 shows the response of the heaviest and the lightest specimen in a spider chart where the four axes are LCF cycles, Z-deflection, Mass, and FOS. In the first chart, mass and distortion are significantly high while LCF cycle is lower than average value in both the charts when compared with all the other specimens.

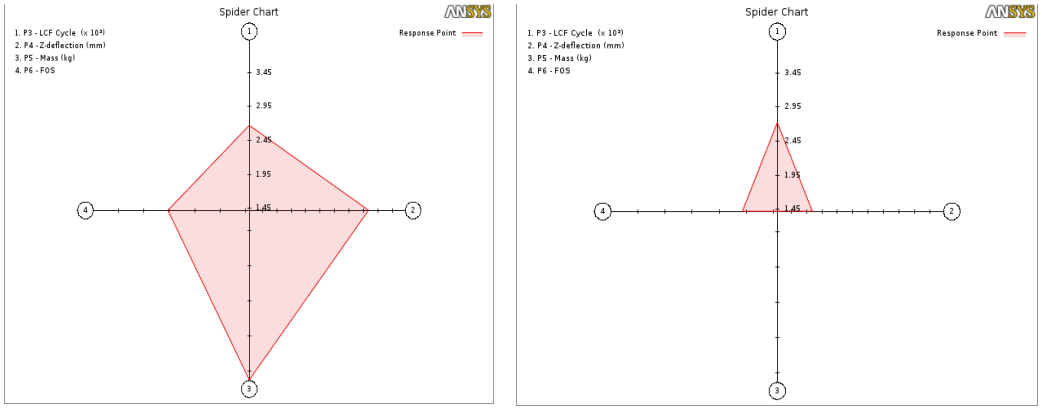

Figure 4-28 Spider graph showing response of the heaviest specimen (left) Vs response of the lightest specimen (right)

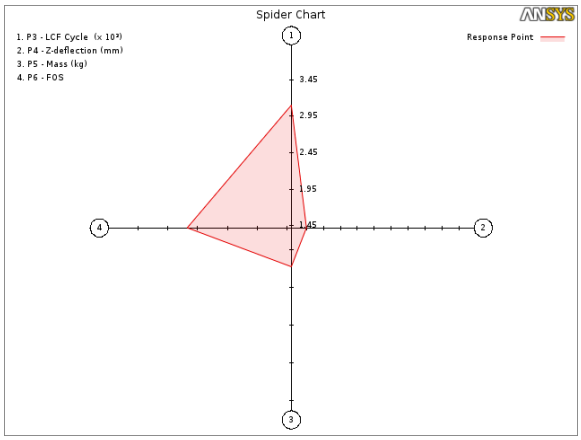

Figure 4-29 Spider chart for the optimum response

Figure 4-29 shows the response of the optimized geometry where z-deformation is reduced to 1.39 mm and LCF cycle is increased to 3210 with mass of 0.02724 kg.

Analysis on the optimized model

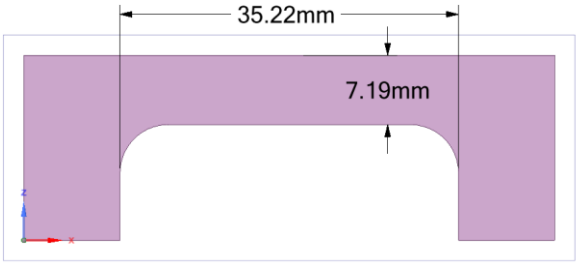

Figure 4-30: Dimensions of the optimized model

The maximum z-deformation obtained from the additive simulation was 1.37 mm while the predicted value was 1.39 mm which is illustrated in figure 4-31.

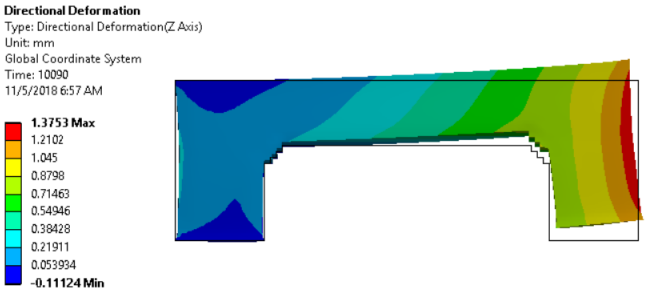

Figure 4-31: Z-deformation from additive simulation

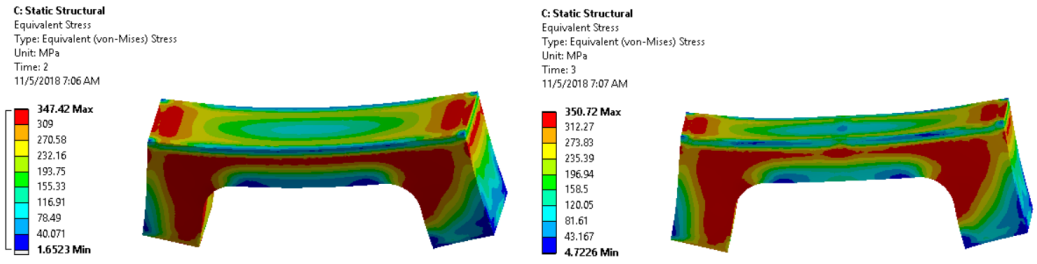

Figure 4-32: Von Mises stress state before (left) and after (right) the superposition [deformations are 5x scaled]

The equivalent stress and strain state before and after the superposition are shown in figure 4-32 and 4-33 respectively. Even though quite large magnitude of load is applied at the middle of the overhang, the stresses does not rise significantly. This could be accounted due to local plastic deformation in the model.

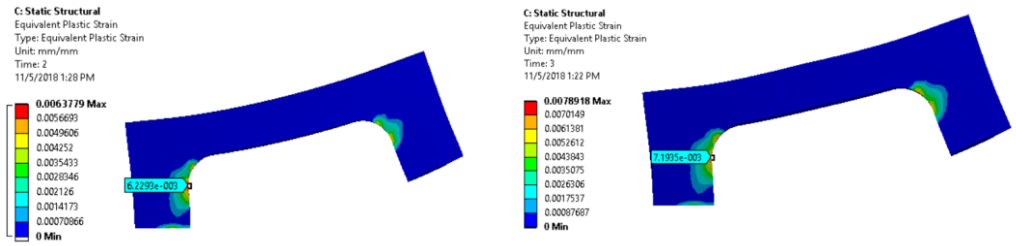

Figure 4-33: Equivalent plastic strain state before (left) and after (right) the superposition [deformations are 10x scaled]

With plastic strain amplitude, $\Delta\varepsilon_p = 1.11E-03\ mm/mm$, the fatigue life calculated from Coffin Manson's equation is 3349 number of plastic strain cycles while the predicted value from the optimization run was 3210 cycles.

4.6.2 Gradient based method for design optimization

The optimization problem for gradient based approach ought to have one single objective with other parameters defined as constraints. The objective and constraints were defined as following:

1) Minimize mass function
2) LCF cycle $\geq$ 3000
3) 1.3 $\leq$ Z-deformation (from additive simulation) $\leq$ 1.4
4) 1.5 $\leq$ FOS $\leq$ 2.6

The optimization problem was run in response surface optimization tab of ANSYS Workbench and also with a MATLAB code. The iterative process converged with only 21 evaluations with optimum point L = 35mm and T = 7.052 mm. The percentage differences from the optimum point predicted from MOGA is 0.61% for length and 1.89% for thickness.

Chapter 5

Conclusion

The work presented gives an insight to using the equations representing few detrimental effects of metal additive manufacturing like the residual stresses, deformations, and fatigue life into leveraging design optimization of critical load bearing structure. The important findings of the current work are summarized with the following points:

- All the specimens were subjected to higher than yield residual stresses post build which is due to the $\alpha\Delta T$ strains. After removal of the supports and the base plate, the peak stresses primarily in x and z directions reduces in all the specimens to almost equal stress level producing different magnitudes of deformation.
- The main effect curve in 3 levels of length with constant thickness had relatively more influence on distortion than the curve with 3 levels of thickness and constant length. It can thus be inferred that the distortion of the part in z-direction is more dependent on length than thickness of the specimen. Also, no interaction of length and thickness could be seen when the combined effect was analyzed.
- The main effect curve for fatigue life in 3 levels of length with constant thickness and 3 levels of thickness with constant length elucidates that both length and thickness have substantial effects. These influences are however, exactly opposite i.e. increasing length with constant thickness decreases fatigue life and vice versa. Furthermore, slight interaction among length and thickness is observed for the calculated values of fatigue life.
- The objective equations to be maximized and minimized for LCF life and deformations respectively, were successfully predicted in full quadratic form using linear regression approach. The advantage of full quadratic equation over linear is that the curvatures (if present) in the response surface can be properly identified

which in turn also increases accuracy of the predicted parameter. This can be analyzed with the predicted coefficient of determination for distortion, fatigue life and factor of safety all of which were either approximately equal to 1 or exactly 1.

- The optimum length and thickness values of the specimens which are factors considered in the DOE study are found to be 35.216 mm and 7.188 mm respectively from the MOGA algorithm which converged after 669 evaluations. The response provided by this set of dimensions is enlisted below:
    a. The overall mass is 60% lower when compared to the heaviest specimen.
    b. The low cycle fatigue life is only 20% lower than the specimen that offered the highest life.
    c. The z-deformation that occurs post removal of supports and base plate is 41% lower than the specimen showing largest deformation.
- The optimum point was also predicted using nonlinear multivariable gradient based algorithm where single objective function of mass was minimized with all other parameters defined as constraints. This optimization run converged with only 21 evaluations and the percentage difference seen from MOGA run was only 0.61% and 1.89% for length and thickness respectively which are miniature differences. Hence, it can be concluded that gradient based algorithm was computationally efficient for this problem when compared with genetic algorithm.

Chapter 6

Future Study and Recommendations

The bridge specimens have been fabricated and are currently in process to be cut off from the base plate after which the deformations and stress state predicted from the current study will be compared with the actual experimental results. However, there are some limitations of the current work which should be taken into consideration or amended when the findings are considered for any further study which are enlisted below:

- It should be taken into account that one of the ends of the specimen after removal from the baseplate was fixed so that other end could deform which is the cause of asymmetrical stress distribution. This could be a possible result if the cutting process is gradual along the horizontal direction, however, a swift cut may result in symmetrical stress pattern unlike the results obtained from the current study.
- It can be seen in figure 4-17 that there is a presence of discontinuity in unaveraged plastic strains along the adjacent elements which infers that the strains have not converged. Mesh density analysis and adaptive mesh refinement was not performed in this study because of limited computational capacity of the system where ANSYS Additive suite was installed. Due to this, it is necessary to ensure convergence of stresses and strains before the results are used for any future comparisons.
- The fatigue model assumed in the current study is rather simplified approach addressing the effect of residual stresses based on plastic strains with no account of size and distribution of the defects. Subsequently, the model also needs to be modified in order to take mean stress and crack closure effects into consideration. All these effects if encompassed with a probabilistic approach would result in a more realistic life prediction than deterministic approach.

- A more powerful tool ‘Additive Science’ has the capability to predict melt pool characteristics, defect density and the microstructure at any location and time during the build process. Parametric study of all these properties is essential to analyze their impact on structural response of the fabricated component.

Appendix A

MATLAB Code

MOGA

```
%%Defining objective functions
function f = objfcn(guess)
k = zeros(2,1); % Make a matrix of size 2x1 and fill it with zeroes
X = guess(1); % take the population and specify X and Y from the population
Y = guess(2); % guess set
%% Objective functions
% Mass Objective
k(1) = 0.0105+(1.8185E-06*X)+(8.3507E-04*Y)-(1.8519E-08*(X^2))+(3.7333E-
07*(Y^2))+(4.2E-05*X*Y);
% Fatigue Objective multiplied by -1 to be minimized, so essentially a maximization
k(2) = -1*(5859.3-(98.5426*X)-(229.8*Y)+((X^2)*0.5170)+((Y^2)*29.6533)+(X*Y*0.58));
f=k;
end

%%Defining system constraints
function [g,heq] = constfcn(guess)
X = guess(1); % take the population and specify X and Y from the population
Y = guess(2); % guess set
%% Constraints
% Factor of Saftey Function
FOS = 0.6519-(0.0683*X)+(0.6907*Y)+(7.2593E-04*(X^2))-(0.0011*(Y^2))-(0.0055*X*Y);
% Deflection Function
def = 1.2565+(0.0242*X)-(0.1587*Y)+(3.70E-05*(X^2))+(0.0077*(Y^2))-(6.67E-05*X*Y);
%% 1.5 <= FOS <= 2.7
g1 = 1-(FOS/1.5);
```

```
g2 = (FOS/2.7)-1;
%% 1.3<=def<=2.4
g3 = 1-(def/1.3);
g4 = (def/1.4)-1;
%% Specify G & HEQ as constraints
heq = 0;
g = [g1;g2;g3;g4];
end

%%Optimization Execution
clear;
clc;
% Bounds
UB = [65 10];   % Upper Bound
LB =[35 5];     % Lower Bound
NVARS = 2;      % Population Size
Aeq = [];
Beq = [];
A   = [];
B   = [];
% Call Objective and Contraints
OBJ = @objfcn;
CONS = @constfcn;
% Optimization options to show iteration
OP = optimoptions('gamultiobj','Display','iter');
% Call Optimizer to run the MOGA
```

XOPT = gamultiobj(OBJ,NVARS,A,B,Aeq,Beq,LB,UB,CONS,OP);

Fmincon Optimizer

```
%%obj function
function f = objfcn(guess)
%k = zeros(2,1); % Make a matrix of size 2x1 and fill it with zeroes
X = guess(1); % take the population and specify X and Y from the population
Y = guess(2); % guess set
%% Objective functions
% Mass Objective
k = 0.0105+(1.8185E-06*X)+(8.3507E-04*Y)-(1.8519E-08*(X^2))+(3.7333E-
07*(Y^2))+(4.2E-05*X*Y);
f=k;
end
function [g,heq] = constfcn(guess)
global hist
X = guess(1); % take the population and specify X and Y from the population
Y = guess(2); % guess set
%% Constraints
% Factor of Saftey Function
FOS = 0.6519-(0.0683*X)+(0.6907*Y)+(7.2593E-04*(X^2))-(0.0011*(Y^2))-(0.0055*X*Y);
% Deflection Function
def = 1.2565+(0.0242*X)-(0.1587*Y)+(3.70E-05*(X^2))+(0.0077*(Y^2))-(6.67E-05*X*Y);
%Fatigue Life
fati = (5859.3-(98.5426*X)-(229.8*Y)+((X^2)*0.5170)+((Y^2)*29.6533)+(X*Y*0.58));
%% 1.5 <= FOS <= 2.6
```

```
g1 = 1-(FOS/1.5);

g2 = (FOS/2.6)-1;

%% 1.3<=def<=1.4

g3 = 1-(def/1.3);

g4 = (def/1.4)-1;

g5 = 1-(fati/3000);

%% Specify G & HEQ as constraints

heq =0;

g = [g1;g2;g3;g4;g5];

c2 = [FOS,def,fati];

hist = [hist;c2];

end

%% ==================Main Execuation Code==========================

clear;

clc;

global his;

his=[];

% Bounds

UB = [65 10];   % Upper Bound

LB =[35 5];     % Lower Bound

NVARS = 2;      % Population Size

Aeq = [];

Beq = [];

A   = [];

B   = [];
```

```
% Call Objective and Contraints

OBJ = @objfcn;

CONS = @constfcn;

% Optimization options to show iteration

OP = optimoptions('gamultiobj','Display','iter');

OPFMINCON = optimset('disp','iter');

% Call Optimizer to run the MOGA

%XOPT = gamultiobj(OBJ,NVARS,A,B,Aeq,Beq,LB,UB,CONS,OP);

[XOPTf,fevalx] = fmincon(OBJ,[36 6],A,B,Aeq,Beq,LB,UB,CONS,OPFMINCON);
```

Bibliography

Ambriz, R. R., & Jaramillo, D. (2014). Mechanical behavior of precipitation hardened aluminum alloys welds. *In Light Metal Alloys Applications*, InTech.

Anderson, T. L. (2017). *Fracture mechanics: fundamentals and applications.* CRC press.

ANSYS®. (2018). Retrieved from Academic Research Mechanical, Release 19.1, Multi-Objective Genetic Algorithm (MOGA), Help System, ANSYS, Inc.

ASTM-E606/E606M-12. (2012). *Standard test method for strain-controlled fatigue testing.* ASTM international, West Conshohocken (PA USA): Book of Standards, 3.

Attaran, M. (2017). The rise of 3-D printing: The advantages of additive manufacturing over traditional manufacturing. *Business Horizons*, 60(5), 677-688.

Benedetti, M., Fontanari, V., Bandini, M., Zanini, F., & Carmignato, S. (2018). Low-and high-cycle fatigue resistance of Ti-6Al-4V ELI additively manufactured via selective laser melting: Mean stress and defect sensitivity. *International Journal of Fatigue, 107*, 96-109.

Bian, L., Thompson, S. M., & Shamsaei, N. (2015). Mechanical properties and microstructural features of direct laser-deposited Ti-6Al-4V. *Jom, 67(3)*, 629-638.

Brackett, D., Ashcroft, I., & Hague, R. (2011). Topology optimization for additive manufacturing. *In Proceedings of the solid freeform fabrication symposium, Vol.1* (pp. 348-362). Austin, TX: S.

Buchbinder, D., Meiners, W., Pirch, N., Wissenbach, K., & Schrage, J. (2014). Investigation on reducing distortion by preheating during manufacture of aluminum components using selective laser melting. *Journal of Laser Applications, 26(1)*, 012004.

Chennakesava, P., & Narayan, Y. S. (2014). Fused deposition modeling-insights. *Proceedings of the International Conference on Advances in Design and Manufacturing ICAD&M (Vol.14)*, (pp. 1345-1350).

Dieter, G. E., & Bacon, D. J. (1986). Residual Stresses. In *Mechanical metallurgy (Vol. 3)* (p. Chapter 15). New York: McGraw-hill.

Edwards, P., & Ramulu, M. (2014). Fatigue performance evaluation of selective laser melted Ti–6Al–4V. *Materials Science and Engineering: A, 598*, 327-337.

Ekmekçi, B., Ekmekçi, N., Tekkaya, A., & Erden, A. (2004). Residual stress measurement with layer removal method. *Meas. Tech, 1*, 3.

Fulcher, B. A., Leigh, D. K., & Watt, T. J. (2014). Comparison of AlSi10Mg and Al 6061 processed through DMLS. *In Proceedings of the Solid Freeform Fabrication (SFF) Symposium*, (p. Vol. 46). Austin, TX, USA.

GE jet engine bracket challenge. (2013). Retrieved from https://grabcad.com/challenges/ge-jet-engine-bracket-challenge

Gharizadeh, A., Samali, B., & Saleh, A. (2013). Investigation of Residual Stress Effect on Fatigue Life of Butt Weld Joints Subjected to Cyclic Bending.

Gibson, I., Rosen, D., & Stucker, B. (2015). *Additive Manufacturing Technologies 3D Printing, Rapid Prototyping, and Direct Digital Manufacturing Second Edition.* Springer.

Gong, H., Rafi, K., Gu, H., Starr, T., & Stucker, B. (2014). Analysis of defect generation in Ti–6Al–4V parts made using powder bed fusion additive manufacturing processes. *Additive Manufacturing, 1*, 87-98.

Gorelik, M. (2017). Additive manufacturing in the context of structural integrity. *International Journal of Fatigue, 94*, 168-177.

Greving, D. J., Rybicki, E. F., & Shadley, J. R. (1994). Through-thickness residual stress evaluations for several industrial thermal spray coatings using a modified 101 layer-removal method. *Journal of Thermal Spray Technology, vol. 3, no. 4*, 379–388.

Gu, D. D., Meiners, W., Wissenbach, K., & Poprawe, R. (2012). Laser additive manufacturing of metallic components: materials, processes and mechanisms. *International materials reviews, 57(3)*, 133-164.

Inaekyan, K., Paserin, V., Bailon-Poujol, I., & Brailovski, V. (2016). Binder-jetting additive manufacturing with water atomized iron powders. *AMPM 2016 Conference on Additive Manufacturing*, (pp. 5-7). Boston.

inc, A. (2018, August 14). *ANSYS Additive Solutions by Dr. Brent Stucker, Additive Director, ANSYS*. Retrieved from https://www.youtube.com/watch?v=e5axGYP1YNw

Kobryn, P. A., & Semiatin, S. L. (2001). Mechanical properties of laser-deposited Ti-6Al-4V. *In Solid Freeform Fabrication Proceedings*, (pp. 6-8). Austin.

Konak, A., Coit, D. W., & Smith, A. E. (2006). Multi-objective optimization using genetic algorithms: A tutorial. *Reliability Engineering & System Safety, 91(9)*, 992-1007.

Leggatt, R. (2008). Residual Stresses in welded structures. *International Journal of Pressure Vessels and Piping 85(3)*, 144-151.

Levkulich, N. C. (2017). *An Experimental Investigation of Residual Stress Development during Selective Laser Melting of Ti-6Al-4V .* (Doctoral dissertation, Wright State University).

Li, R., J., L., Shi, Y., Wang, L., & Jiang, W. (2012). Balling behavior of stainless steel and nickel powder during selective laser melting process. *The International Journal of Advanced Manufacturing Technology*, 59(9-12), 1025-1035.

Mahmoudi, M., Elwany, A., Yadollahi, A., Thompson, S. M., Bian, L., & Shamsaei, N. (2017). Mechanical properties and microstructural characterization of selective laser melted 17-4 PH stainless steel. *Rapid Prototyping Journal, 23(2)*, 280-294.

Masubuchi, K. (2013). *Analysis of welded structures: residual stresses, distortion, and their consequences (Vol. 33).* Elsevier.

Mercelis, P., & Kruth, J. P. (2006). Residual stresses in selective laser sintering and selective laser melting. *Rapid prototyping journal, 12(5)*, 254-265.

Miao, H. Y., Demers, D., Larose, S., Perron, C., & Lévesque, M. (2010). Experimental study of shot peening and stress peen forming. *Journal of Materials Processing Technology, 210(15)*, 2089-2102.

Montgomery, D. C. (2017). *Design and analysis of experiments.* John wiley & sons.

Mullen, L., Stamp, R. C., Brooks, W. K., Jones, E., & Sutcliffe, C. J. (2009). Selective Laser Melting: A regular unit cell approach for the manufacture of porous, titanium, bone in-growth constructs, suitable for orthopedic applications. *Journal of Biomedical Materials Research Part B: Applied Biomaterials: An Official Journal of The Society for Biomaterials, The Japanese Society for Biomaterials, and The Australian Society for Biomaterials and the Korean Society for Biomaterials, 89(2)*, 325-334.

Narender, K., Rao, A. S., Rao, K. G., & Krishna, N. G. (2013). Temperature dependence of density and thermal expansion of wrought aluminum alloys 7041, 7075 and 7095 by gamma ray attenuation method. *Journal of Modern Physics, 4(3)*, 331-336.

Oehlert, G. W. (2000). *Design and analysis of experiments: Response surface design.* New York: W.H. Freeman and Company.

Pagliaro, P., Prime, M., Clausen, B., Lovato, M., Robinson, J., Schajer, G., . . . Zuccarello, B. (2008). Mapping multiple residual stress components using the contour method and superposition. *In ICRS-8-International Conference on Residual Stresses (Vol. 52)*, (pp. 1-8).

Pal, D., Patil, N., Zeng, K., & Stucker, B. (2014). An integrated approach to additive manufacturing simulations using physics based, coupled multiscale process modeling. *Journal of Manufacturing Science and Engineering, 136(6)*, 061022.

Prevey, P. S. (1986). X-ray diffraction residual stress techniques. *ASM International, ASM Handbook., 10*, 380-392.

Prime, M. B. (2009). The contour method: a new approach in experimental mechanics. *In Proceedings of the SEM Annual Conference.*

Protasov, C. E., Safronov, V. A., Kotoban, D. V., & Gusarov, A. V. (2016). Experimental study of residual stresses in metal parts obtained by selective laser melting. *Physics Procedia, 83*, 825-832.

Roberts, J. L. (2002). *Residual Stress Effects on Fatigue Life via the Stress Intensity Parameter, K.* PhD dissertation, University of Tennessee.

Sandhya, R., Veeramani, A., Rao, K. B., & Mannan, S. L. (1994). On specimen geometry effects in strain-controlled low-cycle fatigue. *International journal of fatigue, 16(3)*, 202-208.

Shrestha, R., Simsiriwong, J., Shamsaei, N., Thompson, S. M., & Bian, L. (2016). Effect of Build Orientation on the Fatigue Behavior of Stainless Steel 316L Manufactured Via A Laser-Powder Bed Fusion Process. *In 27th Annual Solid Frefform Fabrication Symposium Proceedings*, (pp. 605-616).

Siemens. (2017). *Additive manufacturing: Facts and forecasts*. Retrieved from https://www.siemens.com/innovation/en/home/pictures-of-the-future/industry-and-automation/Additive-manufacturing-facts-and-forecasts.html

Skoog, S. A., Goering, P. L., & Narayan, R. J. (2014). Stereolithography in tissue engineering. *Journal of Materials Science: Materials in Medicine, 25(3)*, 845-856.

Strantza, M., Ganeriwala, R. K., Clausen, B., Phan, T. Q., Levine, L. E., Pagan, D., . . . Brown, D. W. (2018). Coupled experimental and computational study of residual stresses in additively manufactured Ti-6Al-4V components. *Materials Letters, 231*, 221-224.

Summers, P. T., Chen, Y., Rippe, C. M., Allen, B., Mouritz, A. P., Case, S. W., & Lattimer, B. Y. (2015). Overview of aluminum alloy mechanical properties during and after fires. *Fire Science Reviews, 4(1), 3*.

Suryawanshi, J., Prashanth, K. G., & Ramamurty, U. (2017). Tensile, fracture, and fatigue crack growth properties of a 3d printed maraging steel through selective laser melting. *Journal of Alloys and Compounds, 725*, 355-364.

Three-level full factorial designs. (n.d.). Retrieved from https://www.itl.nist.gov/div898/handbook/pri/section3/pri339.htm

Uddin, S. Z., Espalin, D., Mireles, J., Morton, P., Terrazas, C., Collins, S., . . . Wicker, R. (2016). Laser powder bed fusion fabrication and characterization of crack-free aluminum alloy 6061 using in-process powder bed induction heating. *In Solid Free. Fabr. Symp*, (pp. 214-227).

Vayre, B., Vignat, F., & Villeneuve, F. (2012). Designing for additive manufacturing. *Procedia CIrP, 3*, 632-637.

Vrancken, B. (2016, June). Study of residual stresses in selective laser melting. *Dissertation presented in partial fulfillment of the requirements for the degree of Doctor in Engineering Science*. ARENBERG DOCTORAL SCHOOL .

Wang, F. (2012). Mechanical property study on rapid additive layer manufacture Hastelloy® X alloy by selective laser melting technology. *The International Journal of Advanced Manufacturing Technology, 58(5-8)*, 545-551.

Webster, G. A., & Ezeilo, A. N. (2001). Residual stress distributions and their influence on fatigue lifetimes. *International Journal of Fatigue, 23*, 375-383.

Withers, P. J. (2007). Residual stress and its role in failure. *Reports on progress in physics, 70(12)*, 2211.

Withers, P. J., & Bhadeshia, H. K. (2001). Residual stress. Part 2–Nature and origins. *Materials science and technology, 17(4)*, 366-375.

Wu, M. W., Chen, J. K., Lin, B. H., & Chiang, P. H. (2017). Improved fatigue endurance ratio of additive manufactured Ti-6Al-4V lattice by hot isostatic pressing. *Materials & Design, 134*, 163-170.

Xing, W., Ouyang, D., Li, N., & Liu, L. (2018). Estimation of Residual Stress in Selective Laser Melting of a Zr-Based Amorphous Alloy. *Materials 11.8*, 1480.

Yadollahi, A., & Shamsaei, N. (2017). Additive manufacturing of fatigue resistant materials: Challenges and opportunities. *International Journal of Fatigue, 98*, 14-31.

Yadollahi, A., Shamsaei, N., Thompson, S. M., & Seely, D. W. (2015). Effects of process time interval and heat treatment on the mechanical and microstructural properties of direct laser deposited 316L stainless steel. *Materials Science and Engineering: A, 644*, 171-183.

Yadollahi, A., Shamsaei, N., Thompson, S. M., Elwany, A., & Bian, L. (2017). Effects of building orientation and heat treatment on fatigue behavior of selective laser melted 17-4 PH stainless steel. *International Journal of Fatigue, 94*, 218-235.

Yap, C. Y., Chua, C. K., Dong, Z. L., Liu, Z. H., Zhang, D. Q., Loh, L. E., & Sing, S. L. (2015). Review of selective laser melting: Materials and applications. *Applied physics reviews, 2.4*, 041101.

Yap, Y. L., Wang, C., Sing, S. L., Dikshit, V., Yeong, W. Y., & Wei, J. (2017). Material jetting additive manufacturing: an experimental study using designed metrological benchmarks. *Precision Engineering 50*, 275-285.

Zaeh, M. F., & Branner, G. (2010). Investigations on residual stresses and deformations in selective laser melting. *Production Engineering, 4(1)*, 35-45.